Journal of Theoretical Biology 386 (2015) 89–104

Contents lists available at ScienceDirect

Journal of Theoretical Biology

journal homepage: www.elsevier.com/locate/yjtbi

A multi-scale mathematical modeling framework to investigate anti-viral therapeutic opportunities in targeting HIV-1 accessory proteins

Gajendra W. Suryawanshi [a,b], Alexander Hoffmann [a,b,*]

[a] Signaling Systems Laboratory, San Diego Center for Systems Biology (SDCSB) and the HIV Interaction Network Team (HINT), UCSD, La Jolla, CA 92093, USA
[b] Institute for Quantitative and Computational Biosciences (QCB) and the Department of Microbiology, Immunology and Molecular Genetics (MIMG), UCLA, Los Angeles, CA 90095, USA

HIGHLIGHTS

- We modeled the contest of HIV-1 accessory proteins and cellular resistance factors.
- To examine their effect on viral dynamics we developed multi-scale models.
- Analytical expressions show how Vpu and Vif inhibition relates to viral extinction.
- Studying combination therapy reveals the potential for pharmacological synergy.

GRAPHICAL ABSTRACT

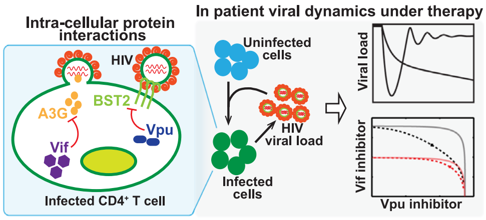

ARTICLE INFO

Article history:
Received 11 April 2015
Received in revised form
13 August 2015
Accepted 31 August 2015
Available online 16 September 2015

Keywords:
Host restriction factors
Combination therapy
Age-structured models
Hypermutations
Reproductive ratio

ABSTRACT

Human immunodeficiency virus-1 (HIV-1) employs accessory proteins to evade innate immune responses by neutralizing the anti-viral activity of host restriction factors. Apolipoprotein B mRNA-editing enzyme 3G (APOBEC3G, A3G) and bone marrow stromal cell antigen 2 (BST2) are host resistance factors that potentially inhibit HIV-1 infection. BST2 reduces viral production by tethering budding HIV-1 particles to virus producing cells, while A3G inhibits the reverse transcription (RT) process and induces viral genome hypermutation through cytidine deamination, generating fewer replication competent progeny virus. Two HIV-1 proteins counter these cellular restriction factors: Vpu, which reduces surface BST2, and Vif, which degrades cellular A3G. The contest between these host and viral proteins influences whether HIV-1 infection is established and progresses towards AIDS. In this work, we present an age-structured multi-scale viral dynamics model of *in vivo* HIV-1 infection. We integrated the intracellular dynamics of anti-viral activity of the host factors and their neutralization by HIV-1 accessory proteins into the virus/cell population dynamics model. We calculate the basic reproductive ratio (R_o) as a function of host–viral protein interaction coefficients, and numerically simulated the multi-scale model to understand HIV-1 dynamics following host factor-induced perturbations. We found that reducing the influence of Vpu triggers a drop in R_o, revealing the impact of BST2 on viral infection control. Reducing Vif's effect reveals the restrictive efficacy of A3G in blocking RT and in inducing lethal hypermutations, however, neither of these factors alone is sufficient to fully restrict HIV-1 infection. Interestingly, our model further predicts that BST2 and A3G function synergistically, and delineates their relative contribution in limiting HIV-1 infection and disease progression. We provide a robust modeling framework for devising novel combination therapies that target HIV-1 accessory proteins and boost antiviral activity of host factors.

---

* Corresponding author at: Institute for Quantitative and Computational Biosciences (QCB) and the Department of Microbiology, Immunology and Molecular Genetics (MIMG), UCLA, Los Angeles CA 90095, USA.
E-mail address: ahoffmann@ucla.edu (A. Hoffmann).

http://dx.doi.org/10.1016/j.jtbi.2015.08.032
0022-5193/

1. Introduction

HIV is the causative agent of the AIDS pandemic. The 2013 UNAIDS report indicates that there are 35.3 million people living with HIV infection, 2.3 million newly HIV-infected people, and 1.6 million AIDS-related deaths in 2012 alone (Fauci et al., 2013). Current anti-HIV drugs target the activity of core retroviral proteins such as Reverse Transcriptase, Integrase and Protease. These drugs have improved life expectancy of HIV infected patients, yet a cure remains elusive, and due to a high retroviral mutation rate for HIV leading to acquired drug resistance, treatment failures are common.

HIV-1 encodes various “accessory proteins” (tat, rev, nef, vif, vpu, vpr and/or vpx), which may not be required for replication *in vitro*, but are critical for HIV's pathogenicity (Malim and Emerman, 2008). Recent studies have revealed that a key function of several accessory proteins is in countering cellular innate immune responses; indeed, several reports have described the molecular mechanisms underlying the contest between host and viral proteins (Malim and Bieniasz, 2012) and thus opened opportunities for the development of new anti-HIV therapeutic strategies targeting HIV-1 accessory protein functions.

The innate immune response is triggered by a variety of pathogen-sensing receptors and comprises a variety of cellular host factors that may control viral progression. Studies of HIV-1 infection, including recent high throughput screens, have identified a number of cellular restriction factors (Brass et al., 2008; Konig et al., 2008; Zhou et al., 2008). Two host restriction factors, BST2 and APOBEC3G (A3G), have been studied extensively in the hope of developing host-factor-based therapeutic strategies. However, HIV-1 uses two accessory proteins, Vpu and Vif, to counter these host factors. These two host restriction factors have been studied using cell culture model systems, which document potent antiviral activity and their mechanisms of action. However, inducing their expression has turned out to be insufficient for sustained anti-viral therapy, as HIV-1 Vpu and Vif counter these host factors. A recent study carried out with HCV/HIV co-infected patients monitored the effect of interferon treatment on HIV viral load and mutagenesis in HIV during the period of the treatment (Pillai et al., 2012). This study provides evidence that interferon enhances the expression of BST2 and APOBEC3 *in vivo* and reduces HIV viral load. However, rebound in viral load showed signs of selective pressure with the emergence of viral populations carrying Vpu variants with greater BST2-neutralizing capacity (Pillai et al., 2012). While these observations are indicative of the anti-viral effects of host resistance factors, they suggest that anti-viral therapies must include targeting of the accessory proteins responsible for neutralizing their activities.

Indeed, other studies suggest that the activity of HIV-1 accessory proteins (e.g. Vif and Vpu) can be hindered by using chemical compounds that interfere with the molecular interactions of viral proteins and host factors (Zuo et al., 2012; Matsui et al., 2014; Mi et al., 2014). For example, small molecules have been identified that restore intracellular A3G levels in infected cells by preventing Vif-induced A3G degradation and reduced production of infectious virus (Matsui et al., 2014). A recent experimental study used a modified peptide BST2-TM-P1 that functions as a competitive binding “decoy” target for Vpu. This competitive binding reduced the effective BST2–Vpu interaction that increased surface BST2 levels and reduced HIV replication (Mi et al., 2014). These experimental studies may justify development of new host factor based anti-viral treatments by targeting the activity of HIV-1 accessory proteins. However, the relationship between *in vitro* results and their *in vivo* potency remains unknown.

Early modeling of HIV infection by Perelson et al. (1996) explored virus turnover rates and the effects of anti-retroviral therapies targeting core HIV-1 proteins. As core proteins are packaged into HIV and the drugs under consideration target them directly, interactions between viral and host factors are excluded in these models. However, a primary function of HIV-1 accessory proteins is to evade the host immune responses; both accessory protein expression and innate responses exhibit intricate kinetics, resulting in changes in viral production over the life of an infected T cell (Mohammadi et al., 2013) i.e. the infection age. In order to connect the age-dependent intracellular interaction kinetics to population level dynamics, age-structured models of HIV-1 dynamics are well suited. Such models have been utilized to incorporate age-dependent HIV-1 production, cell death (Nelson et al., 2004; Gilchrist et al., 2004), and the effects of drug treatments (Kirschner and Webb, 1996). Rong et al. used age-structured models to study the impact of combination antiviral therapy on HIV-1 dynamics (Rong et al., 2007). In their analysis, they calculated the basic reproductive ratio (R_o) to assess the impact of age-dependent virus production and cell death during antiviral therapy. Similar age-structured models have been used to study *in vivo* HCV dynamics to understand the impact of therapeutic targeting of virus–host factor interactions and intracellular viral replication on disease progression (Guedj et al., 2013; Rong et al., 2013). However, these age-structured models do not account for the intracellular processes of accessory protein expression and interaction with host proteins. To incorporate the activity of HIV-1 trans-activator of transcription (Tat) that regulates transcription of HIV-1 in infected cells, Althaus and De Boer developed a multi-scale model (Althaus and de Boer, 2010) . Another study examined intracellular A3G Vif reaction kinetics as HIV-1 infection progresses in cell culture (Hosseini and mac Gabhann, 2012). However, this model is not amenable for describing the dynamics of viral loads or T cell counts in HIV-1-infected individuals. Another computational study proposed an ambitious personalized medicine approach of A3G-augmented stem-cell based gene therapy to control HIV progression (Hosseini and mac Gabhann, 2013). This model did not include the BST2–Vpu axis and cannot be used to study the dynamics of HIV infection when both Vpu and Vif are targeted.

In the current work, we developed age-structured multi-scale models of *in vivo* HIV dynamics to investigate the promise and limitations of accessory protein targeted therapies and to explore the potency of host restriction factors under such therapeutic strategies. We investigated the simultaneous influence of two HIV-1 accessory proteins and host restriction factors interactions, BST2–Vpu and A3G–Vif. Using age-structured multi-scale models, we coupled the intracellular kinetics of these interactions to the cell and virus population dynamics. We calculated the reproductive ratio to examine the impact and sensitivity of key parameters, such as host–viral protein interaction constants, on the progression of viral infection. Combining the two models allowed us to explore predictions on the efficacy of combination therapies targeting both host–viral protein interactions in controlling the spread of the virus *in vivo*. Our results and modeling framework are intended to motivate and inform the development of therapeutic compounds targeting HIV-1 accessory proteins.

2. Results

The results are presented in three parts: we first develop an HIV-1 dynamic model to study the role of the Vpu-induced BST2 downregulation, we then study HIV-1 dynamics as a function of the A3G–Vif interaction, and finally, we combine both BST2 and A3G into a single model to study their combined effect.

2.1. Multi-scale model of BST2 function and HIV-1 dynamics

The restriction factor BST2 is an interferon-induced cellular protein that in some cell types is expressed constitutively (van Damme et al., 2008). It tethers the budding viral particles to the plasma membrane of producer cells, reducing viral production (Neil et al., 2008; Perez-Caballero et al., 2009). BST2 is continuously internalized and recycled to the cell surface, and is also found in other intracellular compartments (Schmidt et al., 2011). Various experimental studies have shown that BST2 is highly efficient in limiting virus release (Gottlinger et al., 1993; Neil et al., 2007). To counter this antiviral activity, HIV-1 has evolved an accessory protein Vpu. HIV-1-Vpu has been shown to down-regulate surface expression of BST2, and release of virus particles is severely reduced in cells infected with Vpu-deleted HIV-1 (Gottlinger et al., 1993; Neil et al., 2007). Some studies suggest that Vpu causes reduction in recycling and synthesis of BST2 (Schmidt et al., 2011; Dube et al., 2011), while others suggest that a direct interaction between Vpu and surface BST2 is responsible for downregulation (McNatt et al., 2013; Mangeat et al., 2009). Vpu may thus be acting at different stages to reduce BST2 surface expression.

We constructed an ordinary differential equations (ODE)-based model of BST2 and Vpu interaction kinetics based on the primary literature. Fig. 1A depicts the possible steps in BST2 transport where Vpu may act to affect BST2 downregulation. As the molecular mechanism of Vpu action remains poorly understood, we employed a generic formulation of Vpu-mediated down regulation of BST2. Equations are as follows:

$$\frac{d}{d\tau}B = \frac{\lambda_B}{1+k_p V_p} - \mu_B B,$$
$$\frac{d}{d\tau}V_p = \lambda_V \frac{\exp(\tau-\tau_1)}{1+\exp(\tau-\tau_1)} - \mu_V V_p, \qquad (1)$$

where B is the surface concentration of BST2, λ_B is the rate at which BST2 is supplied to surface, and μ_B is the rate of removal of BST2 from the plasma membrane. The term $(1+k_p V_p)$ determines

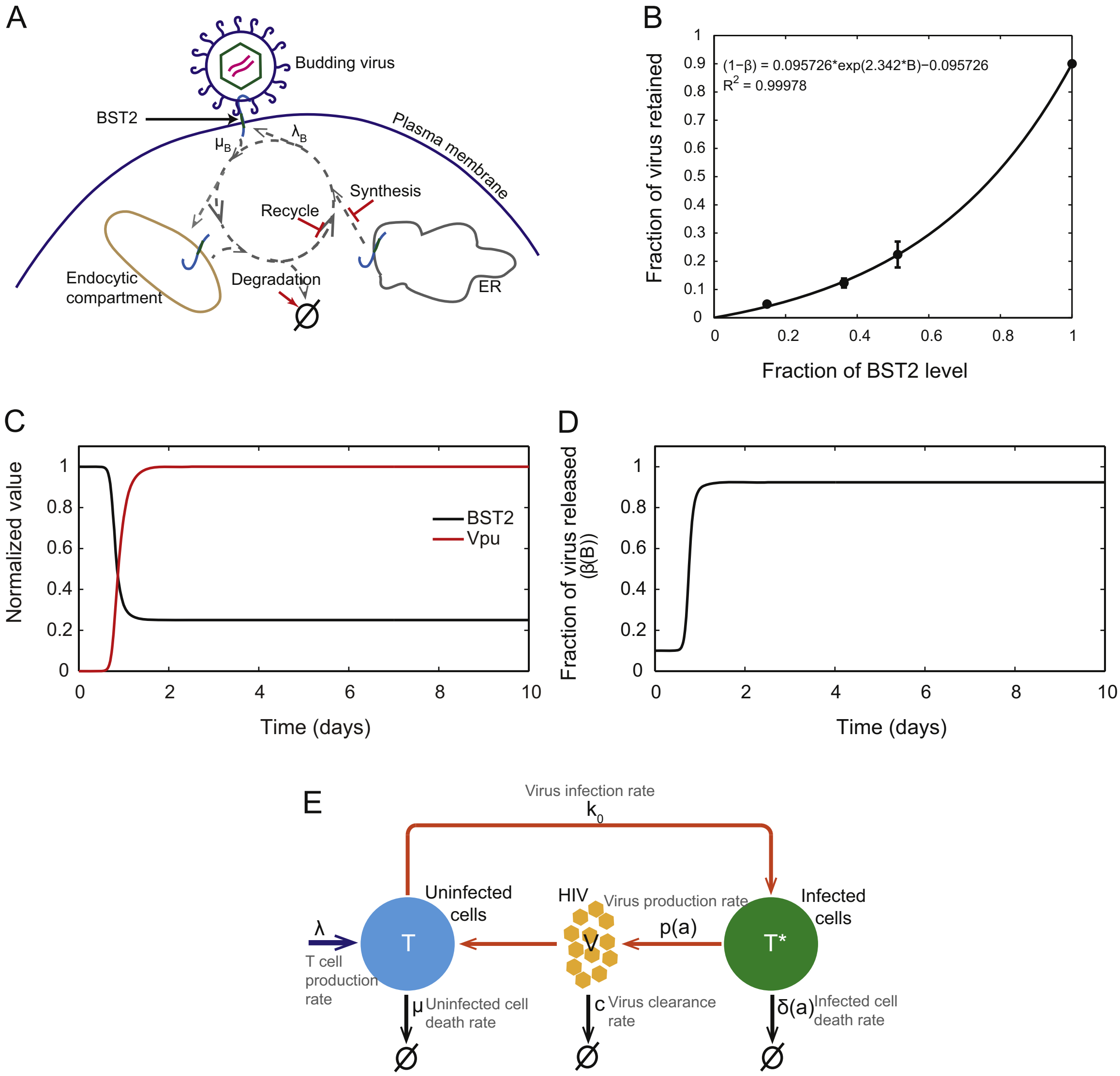

Fig. 1. *HIV-1 replication under the control of BST2 and Vpu.* (A) Schematic of BST2 and Vpu intracellular modes of action. Red arrow indicates enhancement and red blunt arrow represents reduction. (B) Data from experiments (Mangeat et al., 2009) were used to obtain a function to relate the fractional BST2 level to virus restriction efficiency $\beta(B)$. (C) Model simulation of the intracellular dynamics of BST2 and HIV-1-Vpu. HIV-1-Vpu and surface BST2 levels (normalized dimensionless concentrations) are graphed as a function of time in an infected cell. Solution was obtained by solving the equation of BST2–Vpu kinetics (Methods section) with parameter values $\lambda_B = 1.49$/h, $\mu_B = 1.49$/h, $k_p = 3$ (derived from data fitting Supplementary Fig. 1), and $\mu_V = 0.25$/h. (D) Model simulation of viral release $\beta(B)$ from an infected cell as a function of time, reflective of the BST2 and Vpu dynamics graphed in (C). (E) Schematic of key HIV-1 infection events; associated variables are described in the figure. More details about model variables and parameter values are provided in Supplementary Tables.

Vpu-induced (V_p) reduction in the recycling of BST2. We considered that after HIV-1 entry, translation of viral proteins begins around 12–16 h post-entry and reaches a constant production rate around the 24 h mark (Mohammadi et al., 2013). The exponential term in the Vpu equation accounts for the intracellular production of Vpu where λ_V is the maximum constant rate of production of viral protein and μ_V is the degradation rate of viral protein. In these equations, time τ represents the time post-HIV-1 entry into an uninfected T cell and τ_1 is the time required for viral protein translation to reach half the maximum value (we use $\tau_1 = 18$ h). Values for these parameters are taken from the literature (Hosseini and mac Gabhann, 2012), and we assume that both HIV-1-Vpu and HIV-1-Vif have similar production and degradation rates.

The parameters pertaining to BST2 transport were obtained by fitting the model to published data (see Methods section for details). We used experimental data to construct a function of BST2 effectiveness wherein the strength of viral restriction declines exponentially with decreasing BST2 levels (see Methods section). We define $\beta(B)$ to be the fraction of virus released at a given BST2 concentration compared to virus released in the absence of BST2. In this formulation, $(1-\beta(B))$ represents the effectiveness of BST2 in restricting viral release; its value varies between 0 and 1 and is a function of BST2 abundance. Later, $\beta(B)$ is used for connecting the intracellular kinetics to cell population level dynamics. We fitted the BST2 level and virus release experimental data and obtained the following correlation function and its parameters C_1, C_2 and C_3 as shown in Fig. 1B:

$$(1-\beta(B)) = C_1 \times \exp(C_2 \times B) - C_3 \tag{2}$$

The ODE model describes the relationship between BST2 and Vpu levels in an infected cell as a function of infection age and concomitant changes in viral restriction (Fig. 1C and D). The model recapitulates the experimental evidence that Vpu efficiently downregulates and neutralizes the anti-viral action of BST2 (Schmidt et al., 2011; McNatt et al., 2013; Mangeat et al., 2009). Previous work also shows that HIV-Vpu can counteract anti-viral activity of overexpressed, as well as interferon-induced endogenous BST2 (Mangeat et al., 2009). Other studies have shown that mutations in BST2 can impart resistance against Vpu that impede their interactions (Cocka and Bates, 2012; Tokarev et al., 2011). Thus, in the model, the inhibition constant, k_p, which mediates Vpu-induced downregulation of BST2 surface expression, is a key parameter. In an infected cell, as Vpu lowers surface BST2 as a function of the inhibition constant (k_p), the amount of virus released, $\beta(B)$, increases (Fig. 1D).

To study the impact of Vpu function and surface BST2 activity on the fate of HIV-1 infection, we linked the cellular level BST2 action to population level virus-cell dynamics. We began by constructing an age-structured model of HIV-1 infection that describes *in vivo* infection events (Fig. 1E). The model is similar to previous studies (Nelson et al., 2004; Rong et al., 2007; Althaus et al., 2009) and model equations are shown below:

$$\begin{aligned}
&\frac{d}{dt}T = \lambda - \mu T - k_0 V T,\\
&\quad \frac{\partial}{\partial t}T^*(a,t) + \frac{\partial}{\partial a}T^*(a,t) = -\delta(a)T^*(a,t),\\
&\quad \frac{d}{dt}V = \int_0^\infty p(a)T^*(a,t)\,da - cV,\\
&\quad T^*(0,t) = k_0 V T,
\end{aligned} \tag{3}$$

where T is the target cell or uninfected T cell (CD4$^+$ T cell) population, produced at a constant recruitment rate, λ, and has a constant death rate, μ. The virus population, V, infects target cells with a second order infection rate, k_0, and is cleared from the body at rate, c. $T^*(a,t)$ is the population density of infected cells of infection age a at any given time t. Infected cells die at rate $\delta(a)$, and $p(a)$ is the virus production rate of an infected cell of age a. The integral $\int_0^\infty p(a)T^*(a,t)\,da$ is the total number of viruses produced by all infected cells of infection age between 0 and ∞ at a given time t. Given that virus production is a function of the infection age described by Eq. (3), we coupled it with the BST2-induced virus restriction and Vpu-mediated neutralizing effect:

$$p(a) = \begin{cases} \beta(B)p^*(1-e^{-\theta(a-a_1)}) & \text{if } a \geq a_1 \\ 0 & \text{else} \end{cases} \tag{4}$$

where θ (day^{-1}) determines the pace at which viral production reaches saturation level p^*, and a_1 is the age of the infected cell when virus production begins. Again, $\beta(B)$ is the fraction of virus released at a given BST2 concentration compared to virus released in the absence of BST2. Here, $\beta(B)$ links the intracellular BST2–Vpu interaction kinetics to the cell population level dynamics.

2.1.1. *Estimating the basic reproductive ratio*

Steady-state analysis of the system presented in (3) gives two steady states: the infection-free steady state and the infected steady state. For the infected steady state we obtain the following steady state values for key model variables (Nelson et al., 2004)

$$\begin{aligned}
&T^{SS} = \frac{c}{k_0 N}, \quad V^{SS} = \frac{\lambda k_0 N - \mu c}{k_0 c},\\
&\quad N = \int_0^\infty p(a)e^{-\int_0^a \delta(s)\,ds}\,da,
\end{aligned} \tag{5}$$

where, T^{SS} and V^{SS} are the steady-state T cell population and steady-state virus population, respectively. N is the total number of viruses produced by one infected cell over its life span. Details of these calculations are provided in the Methods section. The terms in (5) show that virus infection is sustained as long as $V^{SS} > 0$ which means $(\lambda k_0 N - \mu c) > 0$ or $R_1 > 1$, where

$$R_1 = \frac{\lambda k_0 N}{\mu c} \tag{6}$$

It is apparent that the infected steady state exists only if $R_1 > 1$. We note that λ/μ is the steady-state T cell population in the absence of virus infection, k_0 and c are infection rate and virus clearance rate, respectively. As suggested by Rong et al. (2007) the term (6) gives the number of secondary infections arising from a single infected cell during its entire infectious period in a population of susceptible cells. Hence, we consider R_1 the reproductive ratio under the influence of BST2 and used it to study the impact of Vpu function and surface BST2 activity on the course of HIV-1 infection.

2.1.2. *Influence of reducing Vpu-mediated BST2 degradation on the fate of infection*

Eq. (6) shows that R_1 is directly proportional to the production rate of healthy T cells, their infection rate, and the total number of virus produced per infected cell, N. N is governed by BST2 effectiveness represented by the inhibition constant k_p. In a normal infection, Vpu reduces the BST2 level about four-fold [8,13]; in our model $k_p = 3$ reproduces this observation. For calculating the reproductive ratio R_1, we use the *in vivo* dynamics parameters provided in the literature (Rong et al., 2007). We evaluate the value $p^* = 9.675 \times 10^3$ as we consider that virus production at the cell surface begins at 15–18 h (Mohammadi et al., 2013) (value used for calculations 16 h = 0.66 days) post-HIV-1 entry in the cell and $\theta = 1$, which results in 2500 virions per infected cell (N) as previously suggested by Rong et al. (2007, 2008). The maximum age of an infected cell is considered to be 10 days and the infected cell death rate is assumed to be constant, i.e. independent of infection age. We assume that at the onset of therapy all the cells are expressing BST2 and show Vpu-induced downregulation. To calculate N, we solve the BST2–Vpu model to get the estimate of

$\beta(B)$ and numerically evaluate the integral using Simpson's 1/3 rule.

To study the impact of varying the surface BST2 level on the HIV-1 infection, we calculated the reproductive ratio for different values of the inhibition constant (k_p). Reducing k_p reduces Vpu-induced BST2 downregulation and the surface concentration of BST2 increases (Fig. 2A). Calculations further show that R_1 decreases as we reduce the inhibition constant (Fig. 2B), due to the decreased viral release. Consequently, reducing the inhibition constant causes a drop in the steady-state virus population, V^{SS} (Fig. 2C). Our calculations also show that, to drop the reproductive ratio below 1, k_p value should be less than 0.18. This means that an infected cell must maintain $\approx 85\%$ (≈ 0.85 in fraction) of its pre-infection level of surface BST2, referred to as the "critical surface BST2 level", in order to achieve a reduction in virus release that is sufficient to clear HIV-1 from the system. Conversely, increasing the inhibition constant k_p above its base value of 3 (25% of pre-infection BST2) does not alter the reproductive ratio or the steady state viral load. This suggests that the Vpu effect reaches a limit where the anti-viral activity of BST2 is nullified and virus production proceeds as if there were no BST2 at all.

For the above calculations we kept the total number of viruses produced per infected cell (N) constant. However, the value of N affects how much surface BST2 is required to maintain a reproductive ratio below 1. Investigating this relationship, we find that the "critical surface BST2 level" increases rapidly with increasing viral production, however, at higher viral production levels we approach saturation (Fig. 2D). These results indicate that although the reproductive ratio increases linearly (Eq. (6)) with virus production, the critical surface BST2 level varies non-linearly.

2.1.3. HIV-1 dynamics under BST2–Vpu-targeted treatment

We next pursued numerical solutions of our model to extend the findings of the previous sections and to visualize the time evolution of HIV-1 and T-cell dynamics that determine the course of HIV-1 pathogenesis. To solve the model (3), we use parameter values provided by Rong et al. (2007, 2008). We specify the death rate of an infected cell as $\delta(a) = \delta$, where value of δ is set to 1 day^{-1}. We consider the maximum age of an infected cell to be $a_{max} = 10$ days. For the calculation of $p(a)$ we set $p^* = 9.675 \times 10^3$, $\theta = 1$, and $a_1 = 0.66$ days, these values result in 2500 virions produced per cell for the no treatment condition. The parameters for the BST2–Vpu kinetics are similar to those used for calculating the reproductive ratio.

In order to model Vpu-mediated inhibition of BST2 we started with the initial condition of the steady-state in the absence of treatment. We obtain steady-state values from Eq. (5) setting $\beta(B) = 1$ (no BST2-mediated inhibition). As T cell and virus populations are at steady state, $T^{SS}(a) = k_0 T^{SS} V^{SS} e^{-\delta a}$, and we calculate the steady-state population densities of infected cells of age a (between 0 and a_{max}). The numerical methods used to simulate the model are given in detail in the Methods section. As mentioned earlier, at time zero we assume that all the cells are expressing BST2 and show Vpu-induced downregulation. To study the impact of drugs that reduce the Vpu-induced BST2 downregulation we employ model simulations for two different values of the inhibition constant, k_p. Simulation results show that reducing k_p by 10-fold (from 3 to 0.3) causes a transient perturbation to the dynamical system and then a new steady state (Fig. 3A). For example, the uninfected T cell count sharply increases as the number of new infections drops due to low virus production and, after oscillating, attains a new steady state that is higher than the pre-treatment level. Similarly, the virus population shows a steep initial decline due to a sudden decrease in the virus production that offsets the balance between virus production and immune clearance (Fig. 3A).

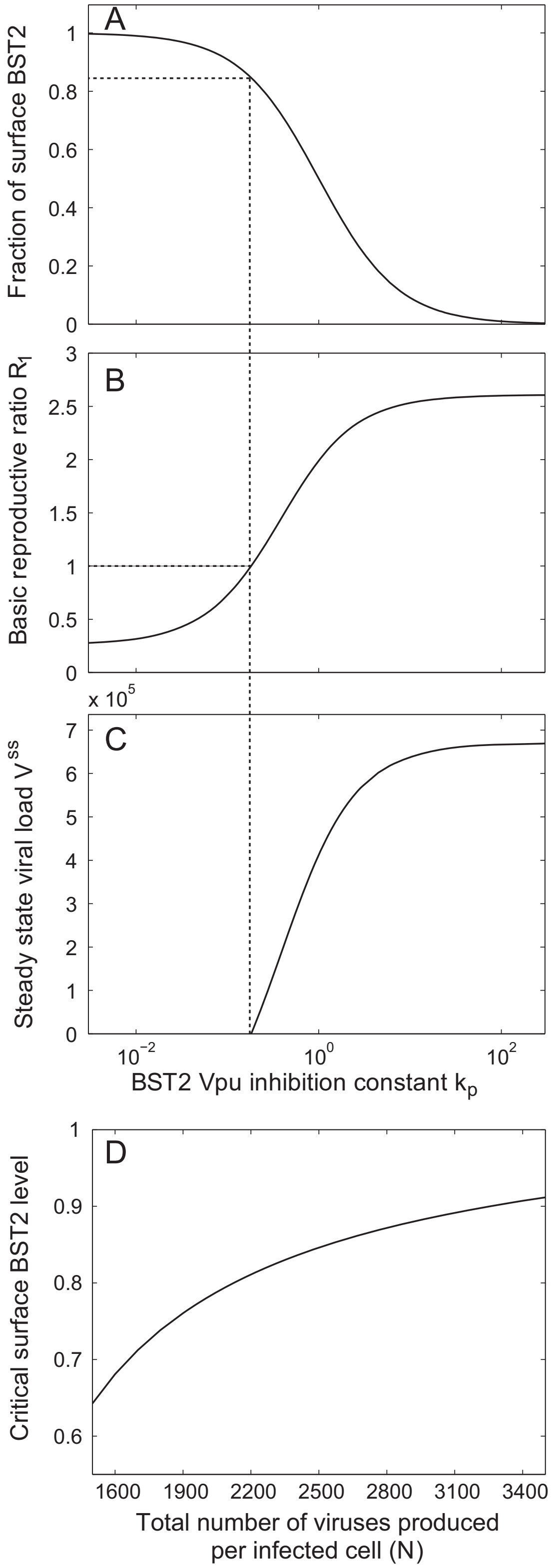

Fig. 2. *The basic reproductive ratio and viral population as a function of the Vpu-induced BST2 downregulation.* (A) Line graph shows the fraction of surface BST2 level in infected cell compared to level in uninfected cell as a function of BST2–Vpu inhibition constant. (B) Graph of the basic reproductive ratio R_1 as a function of the inhibition constant k_p. (C) Graph of steady-state viral load (V^{SS}) as a function of the inhibition constant k_p. The gray dotted lines show V^{SS} value and critical surface BST2 level that reduces R_1 to 1. (D) Graph shows critical surface BST2 level required to reduce $R_1 = 1$ at different per cell virus production. Parameter values used for BST2 and Vpu dynamics were the same as used in Fig. 1 and the parameters used to calculate R_1 and V^{SS} are $\lambda = 10^4$ ml^{-1} day^{-1}, $\mu = 0.01$ day^{-1}, $\delta(a) = 1$ day^{-1}, c = 23 day^{-1}, and $k_0 = 2.4 \times 10^{-8}$ ml^{-1} day^{-1}.

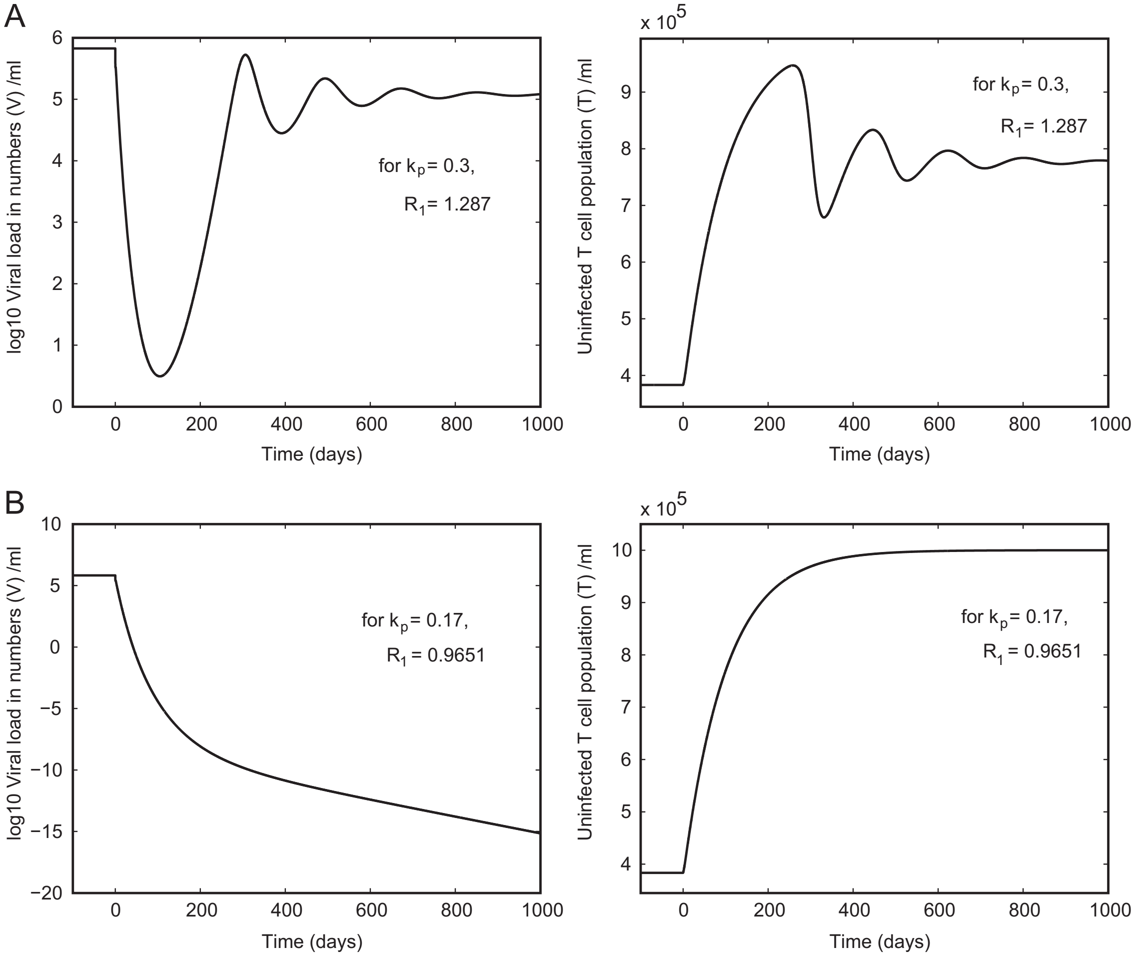

Fig. 3. *HIV-1 and T-cell dynamics following Vpu-BST interaction inhibitor treatment.* (A) *In vivo* time evolution of virus and T cell population following a reduction in k_p but with $R_1 > 1$. (B) *In vivo* time evolution of virus and T cell populations following a reduction in k_p achieving $R_1 < 1$. Simulation results were obtained by solving Eq. (3) using parameter values $\lambda = 10^4$ ml^{-1} day^{-1}, $\mu = 0.01$ day^{-1}, $\delta(a) = 1$ day^{-1}, c = 23 day^{-1}, and $k_0 = 2.4 \times 10^{-8}$ ml^{-1} day^{-1}.

Slowly the new virus production rate matches viral clearance and the system reaches a new steady state that is lower than the pretreatment value. These results show that 10 fold reduction in the value of k_p, the levels of BST2 ($\approx$ 77%) (0.77 in fraction) is not sufficient to terminate viral infection in agreement with our reproductive ratio calculations. When we further reduce the inhibition constant k_p=0.17, which allows surface BST2 levels to rise above critical surface BST2 level of 85% (0.85 in fraction) and provides a reproductive ratio of less than 1, we observe the virus population ultimately dying out and the T cell population bounces back to the infection-free steady-state value (Fig. 3B). These results suggest that BST2-targeted therapy can be effective in controlling an ongoing HIV-1 infection by substantially curtailing Vpu's function.

2.2. Multi-scale model of A3G and HIV-1 dynamics

The host restriction factor, A3G, is expressed constitutively and its expression increases in response to interferon stimulation (Bishop et al., 2004). A3G affects viral replication in two ways. Following packaging of A3G into budding viruses, A3G obstructs the reverse transcription (RT) process (Bishop et al., 2004) and additionally induces hypermutation of the viral genome (Bishop et al., 2004; Mangeat et al., 2003) (Fig. 4A). This interference by A3G not only reduces the probability of successful integration (establishment of a provirus) but also causes an increase in the number of deleterious mutations, resulting in an increased fraction of noninfectious progeny viruses (Mangeat et al., 2003). A3G enters the budding virions resulting in A3G positive progeny viruses. A recent computational population genetics study suggested that 80% of the progeny viruses should incorporate A3G to achieve an effective suppression of the progression of HIV infection *in vivo* (Thangavelu et al., 2014). When these viruses infect target cells, A3G anti-viral activity reduces the possibility of productive replication. The fraction of A3G positive viruses produced by an infected cell depend on the level of A3G expression in the infected cell. HIV-1-Vif opposes the function of A3G by binding to it and accelerating its degradation (Conticello et al., 2003; Sheehy et al., 2003), thereby reducing A3G incorporation into virions. The intracellular A3G–Vif kinetics are key to controlling the dynamics of two virus populations: A3G positive (A3G+) and A3G negative (A3G−). To model these intracellular interactions we used an existing model of A3G–Vif kinetics (Hosseini and mac Gabhann, 2012) and restructured it to fit our requirements. The modified equations are shown below:

$$\frac{d}{d\tau}A = \lambda_A A - \mu_A A - k_{av} A \cdot V_f + k_{va} AV_c,$$
$$\frac{d}{d\tau}V_f = \lambda_V \frac{\exp(\tau - \tau_1)}{(1 + \exp(\tau - \tau_1))} - k_{av} A \cdot V_f + k_{va} AV_c - \mu_V V_f,$$
$$\frac{d}{d\tau}AV_c = k_{av} A \cdot V_f - k_{va} AV_c - \mu_{AV} AV_c, \tag{7}$$

where A is the concentration of A3G produced in the cell at constant rate λ_A and degraded at rate μ_A. V_f is the Vif concentration; Vif

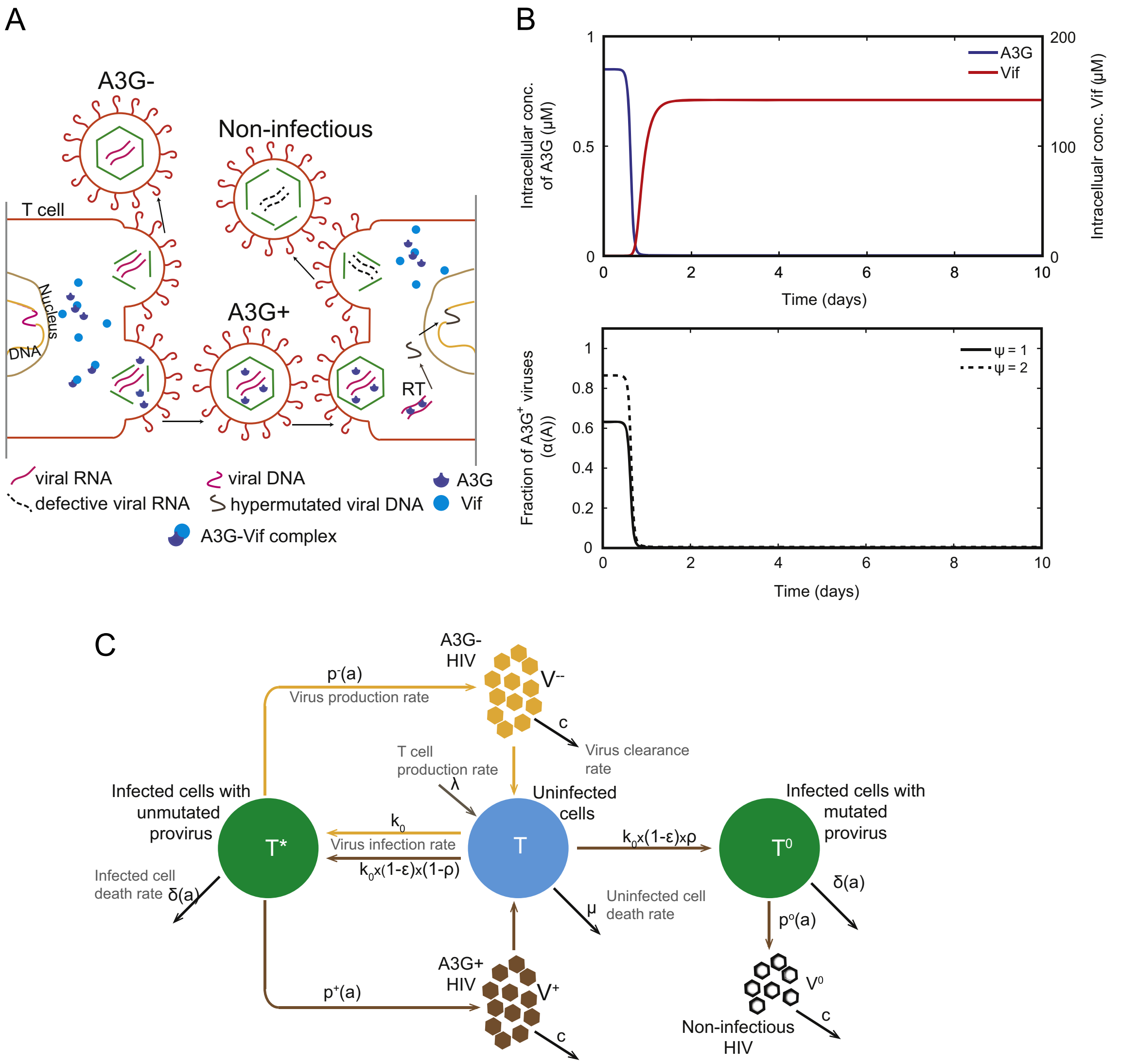

Fig. 4. *HIV-1 replication under the control of A3G and Vif.* (A) Schematic of A3G and Vif intracellular modes of action. (B) A3G and viral kinetics. Top graph shows A3G and Vif intracellular kinetics using parameter values $\lambda_A = 0.085\ \mu\text{M h}^{-1}$, $\mu_A = 0.1\ \text{h}^{-1}$, $\lambda_V = 35.6\ \mu\text{M h}^{-1}$, $\mu_V = 0.25\ \text{h}^{-1}$, $k_{av} = 3600\ \mu\text{M}^{-1}\ \text{h}^{-1}$, $k_{va} = 3600\ \text{h}^{-1}$, $\lambda_{AV} = 0.3\ \text{h}^{-1}$. Bottom graph shows the fraction of A3G+ virus population during the same timecourse. (C) Schematic of key HIV-1 infection events; associated variables are described in the figure. Model details such as variable names and parameter values are provided in Supplementary Tables.

binds A3G with second order rate constant k_{av} and the A3G–Vif complex, AV_c, dissociates at rate k_{va}. Vif is produced and degraded similar to Vpu. μ_{AV} is the degradation rate of the A3G–Vif complex.

Studies have shown that A3G gets packaged into budding virus particles through an intricate route involving interactions of A3G with host proteins, RNAs, viral genomic RNA, and viral proteins (Dussart et al., 2005; Wang et al., 2007; Soros et al., 2007; Alce and Popik, 2004). A recent study posits that A3G surveys the cytoplasm and associates with nascent retroviral RNA to increase its packaging efficiency into virions (Apolonia et al., 2015). It has also been shown that packaging of A3G is proportional to the amount of A3G present in the cell (Xu et al., 2007). This relationship remains poorly understood as packaging of A3G also depends on the concentrations of viral factors such as viral genomic RNA (Khan et al., 2005) and HIV-1 Gag (Schäfer et al., 2004) that vary over infection age. To relate fraction of A3G left in an infected cell and the fraction of budding viruses carrying A3G, we use following exponential function:

$$\alpha(A) = \left(1 - \exp\left(-\psi \frac{A}{A_0}\right)\right) \tag{8}$$

where A_0 is the pre-infection steady state A3G concentration, ψ determines the packaging propensity of A3G and accounts for the efficiency of A3G being packaged into budding virus (Supplementary Fig. 4A shows the behavior of the function). $\alpha(A)$ is the multiplying factor that determines the fraction of A3G+ viruses produced by an infected cell of infection age a with A3G concentration A. Using this relation, we intend to assess the impact of both the change in A3G concentration and the change in its packaging propensity on the inhibition of viral accessory proteins.

Our model recapitulates that the onset of Vif production increases A3G degradation causing a steep decline in the intracellular A3G concentration over the course of the infection (Fig. 4B upper line graph). The fraction of A3G+ virus budding from an infected cell is correlated to the A3G concentration. Hence the fraction of A3G+ viruses produced per cell drop over the course of the infection (Fig. 4B lower line graph). We perform simulations for two different values of ψ, 1 and 2, which result in similar but distinct dynamics of A3G+ and A3G− viruses.

In order to study the consequences of reducing Vif activity and thereby increasing A3G anti-viral activity, we modified the previous model of HIV-1 dynamics as illustrated in Fig. 4C.

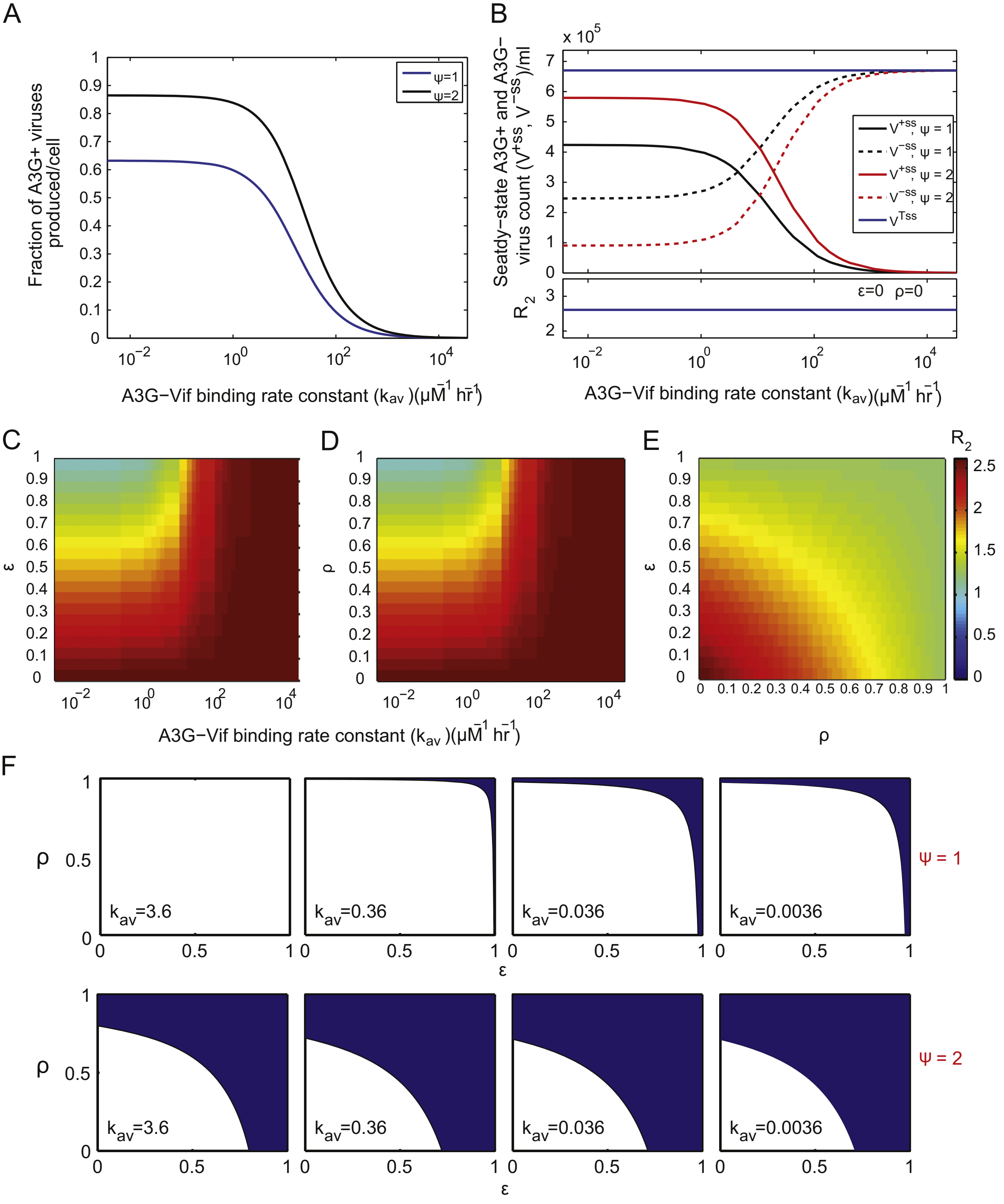

Fig. 5. *The basic reproductive ratio R_2 and virus populations as a function of A3G and HIV-1 Vif.* (A) Shows the change in fraction of A3G+ viruses produced by an infected cell over the life its span as a function of A3G–Vif binding rate constant for different propensity values $\psi=1$ (blue) and 2 (black). (B) Upper panel shows the steady state virus population as a function of k_{av}. Lower panel shows that R_2 does not vary as a function of the A3G–Vif binding rate constant when A3G is not inhibitory. (C) Heatmap showing R_2 as a function of A3G's RT inhibitory activity and the A3G–Vif binding rate constant k_{av}. (D) Heatmap showing R_2 as a function of A3G's hypermutation activity ρ and the A3G–Vif binding rate constant k_{av}. (E) Heatmap showing R_2 as a function of A3G's RT inhibitory activity and its hypermutation activity ρ for a given A3G–Vif interaction with k_{av} kept constant at 3.6 μM^{-1} h^{-1}. (F) Area plots in which the shaded area represents parameter range in which $R_2 < 1$. Each area plot obtained for a binding rate constant value shown in the plot. The calculations were performed for two ψ values 1 (upper panel) and 2 (lower panel). Parameter values used for calculation of R_2 are $\lambda = 10^4$ ml^{-1} day^{-1}, $\mu=0.01$ day^{-1}, $\delta(a)=1$ day^{-1}, $c=23$ day^{-1}, and $k_0 = 2.4 \times 10^{-8}$ ml^{-1} day^{-1}. (For interpretation of the references to color in this figure caption, the reader is referred to the web version of this paper.)

Infected cells produce two types of viruses A3G+ and A3G−. As the A3G+ viruses infect uninfected T cells, A3G (i) interferes with the infection by inhibiting the RT process with a certain efficacy and (ii) introduces lethal mutations to newly transcribed viral DNA with a certain probability. Proviral DNA with lethal mutations produces defective, non-infectious progeny viruses. A3G+ viruses that escape the A3G antiviral activity undergo viral replication with the same rate constants as A3G− viruses.

2.2.1. Model equations

To model the A3G effect on HIV-1 dynamics, we must distinguish between various populations: one uninfected cell population, two

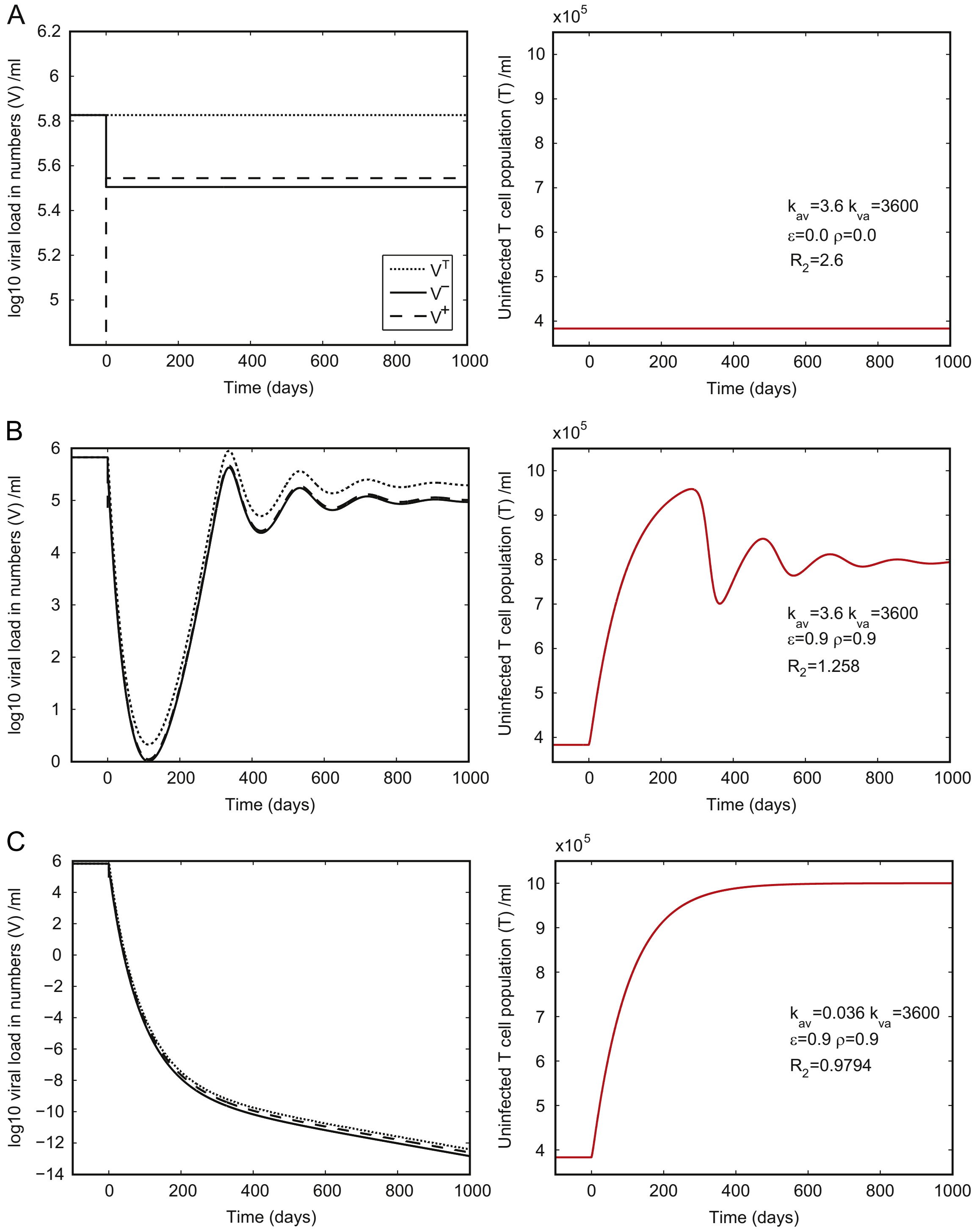

Fig. 6. *Simulations of HIV-1 and T-cell dynamics following A3G–Vif interaction inhibitor treatment.* (A) When A3G has no inhibitory activity ($\rho=\epsilon=0$), a three-fold reduction of the A3G–Vif binding rate constant (k_{av}; at $t=0$) the A3G+ virus population (V^+) increases and A3G− virus (V^-) count drops, causing a change in the composition of viral populations. The emergence of A3G+ virus population in the absence of A3G's inhibitory activity has no influence on the total viral load (V^T) and T cell count (T, right graph). (B) When A3G has inhibitory activity ($\rho=\epsilon=0.9$), a three-fold reduction of the A3G–Vif binding rate constant (k_{av}; at $t=0$) causes transient perturbations in both HIV-1 and T-cell populations and settling into new steady states. (C) Using the same A3G inhibitory activity parameters ($\rho=\epsilon=0.9$), a severe reduction in the A3G–Vif binding rate constant k_{av} can result in clearance of the virus from the system and T-cell population reaches infection-free steady state. The parameters values used to simulate the HIV-1 dynamics model (9) are $\lambda=10^4$ ml^{-1} day^{-1}, $\mu=0.01$ day^{-1}, $\delta(a)=1$ day^{-1}, $c=23$ day^{-1}, and $k_0=2.4\times10^{-8}$ ml^{-1} day^{-1}.

types of infected cell populations, and three kinds of virus populations. We developed the following set of equations:

$$\frac{d}{dt}T=\lambda-\mu T-k_0V^-T-k_0V^+T,$$

$$\frac{\partial}{\partial t}T^*(a,t)+\frac{\partial}{\partial t}T^*(a,t)=-\delta(a)T^*(a,t),$$

$$\frac{\partial}{\partial t}T^0(a,t)+\frac{\partial}{\partial t}T^0(a,t)=-\delta(a)T^0(a,t),$$

$$\frac{d}{dt}V^-=\int_0^\infty p^-(a)T^*(a,t)\,da-cV^-,$$

$$\frac{d}{dt}V^+=\int_0^\infty p^+(a)T^*(a,t)\,da-cV^+,$$

$$\frac{d}{dt}V^0 = \int_0^\infty p^0(a)T^0(a,t)\,da - cV^0,$$
$$T^*(0,t) = k_0V^-T + k_0(1-\epsilon)(1-\rho)V^+T,$$
$$T^0(0,t) = k_0(1-\epsilon)\rho V^+T, \tag{9}$$

where T is again the target/uninfected T cell (CD4$^+$ T cell) population and its production and death are similar to the previous model (3). T cells may be infected by two different virus types V^- viruses or V^+ viruses. The A3G$-$ viruses undergo reverse transcription as in the previous model and hence we can treat the A3G$-$ virus as wild type. In contrast, during A3G$+$ virus infection, the success of the RT step is dependent on the efficacy of A3G. To include this feature, we introduce the term $(1-\epsilon)$, which is the probability of successful RT. In addition, A3G imparts lethal mutations to the proviral DNA during the RT process with a probability ρ that leads to the production of defective/non-infectious viruses, V^0. Thus, the term $(1-\rho)$ gives the fraction of infections by A3G$+$ viruses that produce proviral DNA capable of producing infectious progeny viruses; these virus particles may or may not actually carry A3G. The anti-viral activity of A3G gives rise to two types of infected cell populations T^* and T^0. Here, $T^*(a,t)$ is the infected cell population with infection age, a, which carries a viable provirus at any given time t. These infected cells are produced by A3G$-$ virus infection or by A3G$+$ virus infections in which the RT process escapes A3G's inhibitory and mutational activities. The other infected cell population, $T^0(a,t)$, is defined as the population of A3G$+$ virus infected cells of infection age a at any given time t and carries lethally mutated provirus. Similar to the previous model version (3), $\delta(a)$ is the infection age-dependent death rate of infected cells. As the infected cells produce two distinct types of viruses (depending their A3G status), our new model (9) contains two virus production rates. As the A3G status has no effect on non-infectious viruses, we use the same production rate for these viruses. In system (9), $p^-(a)$ and $p^+(a)$ are the rates at which the infected cell population T^* of infection age a produces A3G$-$ and A3G$+$ viruses, respectively. Values of these rates are as follows:

$$p^-(a) = \begin{cases} (1-\alpha(A))p^*(1-e^{-\theta(a-a_1)}) & \text{if } a \ge a_1 \\ 0 & \text{else} \end{cases}$$
$$p^+(a) = \begin{cases} \alpha(A)p^*(1-e^{-\theta(a-a_1)}) & \text{if } a \ge a_1 \\ 0 & \text{else} \end{cases} \tag{10}$$

where again $\alpha(A)$ is the multiplying factor that determines the fraction of A3G$+$ viruses produced by an infected cell of infection age a with A3G concentration A. The parameters θ and a_1 are the same as in the previous model. The production rate of non-infectious viruses by T^0 can be calculated as follows:

$$p^0(a) = \begin{cases} p^*(1-e^{-\theta(a-a_1)}) & \text{if } a \ge a_1 \\ 0 & \text{else} \end{cases} \tag{11}$$

Using this model, we studied the effect of A3G on the HIV-1 dynamics and the possibility of A3G-mediated therapeutic strategies to control the HIV-1 infection.

2.2.2. *Steady state viral load and reproductive ratio*

In order to derive the reproductive ratio we assume a steady state for the model (9). Variables V^0 and T^0 do not appear in the other equations and are decoupled from the system; hence we can ignore these for the following analysis. As with the previous model, we obtain two steady states: an infection-free steady state and an infected steady state. For the infected steady state we obtain the following relations (details in Methods):

$$T^{SS} = \frac{c}{k_0N_1},$$
$$V^{-SS} = \frac{(\lambda k_0N_1 - \mu c)N_1^-}{k_0c(N_1^- + (1-\epsilon)N_1^+)}, \quad V^{+SS} = \frac{(\lambda k_0N_1 - \mu c)N_1^+}{k_0c(N_1^- + (1-\epsilon)N_1^+)} \tag{12}$$

where N_1^- and N_1^+ are the number of A3G$-$ and A3G$+$ viruses, respectively, produced by an infected cell over its lifespan. These terms are defined as follows:

$$N_1^{\pm} = \int_0^\infty p^{\pm}(a)e^{-\int_0^\infty \delta(s)\,ds}\,da,$$
$$N_1 = N_1^- + (1-\epsilon)(1-\rho)N_1^+ \tag{13}$$

At steady state, for both V^{-SS} and V^{+SS} can attain a non-zero positive value in order to maintain a sustained infection if and only if $(\lambda k_0N_1 - \mu c) > 0$ which, similar to the previous analysis, means $R_2 > 1$ where

$$R_2 = \frac{\lambda k_0N_1}{\mu c} \tag{14}$$

On close inspection of Eq. (14), we propose that R_2 is the reproductive ratio under the effect of A3G. To study the impact of A3G activity on the progression of the HIV-1 infection further, we varied the associated parameters.

2.2.3. *Effect of inhibiting Vif-induced loss of A3G on the reproductive ratio*

Given the multi-step mechanism of A3G antiviral activity, the basic reproductive ratio depends on multiple parameters. The fraction of A3G$+$ virus production depends on the concentration of A3G in an infected cell at the time of virus formation. This concentration depends on the rate at which Vif can bind A3G and target it for degradation. Thus, one of the key parameters that governs the dynamics is the A3G–Vif binding rate, k_{av}. Decreasing the value of this parameter lowers Vif activity and reduces A3G degradation, whereas increasing it has the opposite effect and as a consequence alters the fraction of A3G$+$ viruses released per infected cell (Fig. 5A). In order to examine the effect of A3G–Vif binding alone on the reproductive ratio we varied the value of k_{av}. We kept other parameters constant in Eq. (14) and assumed that A3G had no effect on the RT process ($\epsilon = 0$ and $\rho = 0$). Although reduction of the A3G–Vif binding rate constant increases the A3G$+$ virus population and changes the composition of the A3G$-$ and A3G$+$ virus populations (Fig. 5B top panel), the total number of infectious viruses produced by an infected cell remains constant, as does the number of secondary infections. Hence, R_2 remains constant over the range of k_{av} (Fig. 5B, bottom panel). We performed these simulations for two different values of the packaging propensity parameter (ψ). Though total steady-state virus population and reproductive ratio remain unchanged, for higher values of ψ (i.e. equal to 2) we see an increase in steady-state A3G$+$ virus population compared to lower value of 1.

To further explore whether the increase of the A3G$+$ virus population may have therapeutic benefit we simultaneously varied the binding rate constant k_{av} and A3G's RT inhibition efficacy, ϵ, and calculated the values of R_2 using Eq. (14). The results show that decreasing the binding rates and increasing ϵ reduces the reproductive ratio (Fig. 5C). At very high inhibition and very low binding rate constant, the reproductive ratio value falls below 1. Reducing the binding rate constant (as seen the Fig. 5B) increases the A3G$+$ virus population and due to A3G's RT inhibition activity the number of successful infections is considerably reduced, diminishing the number of infected cells. With fewer cells infected, less virus is produced, which reduced secondary infections as reflected by value of R_2. On the other hand, for high A3G–Vif binding rate constant values, inhibiting the RT efficacy has little effect on R_2 as the total number of A3G$+$ infection is small. A similar effect is observed upon varying both the A3G–Vif binding rate constant and the probability of lethal mutations, ρ (Fig. 5D). To further study the combined effect of RT inhibition ϵ and induction of hypermutation ρ, we set the A3G–Vif binding rate constant at a moderately low value and observed a modest effect on R_2 for

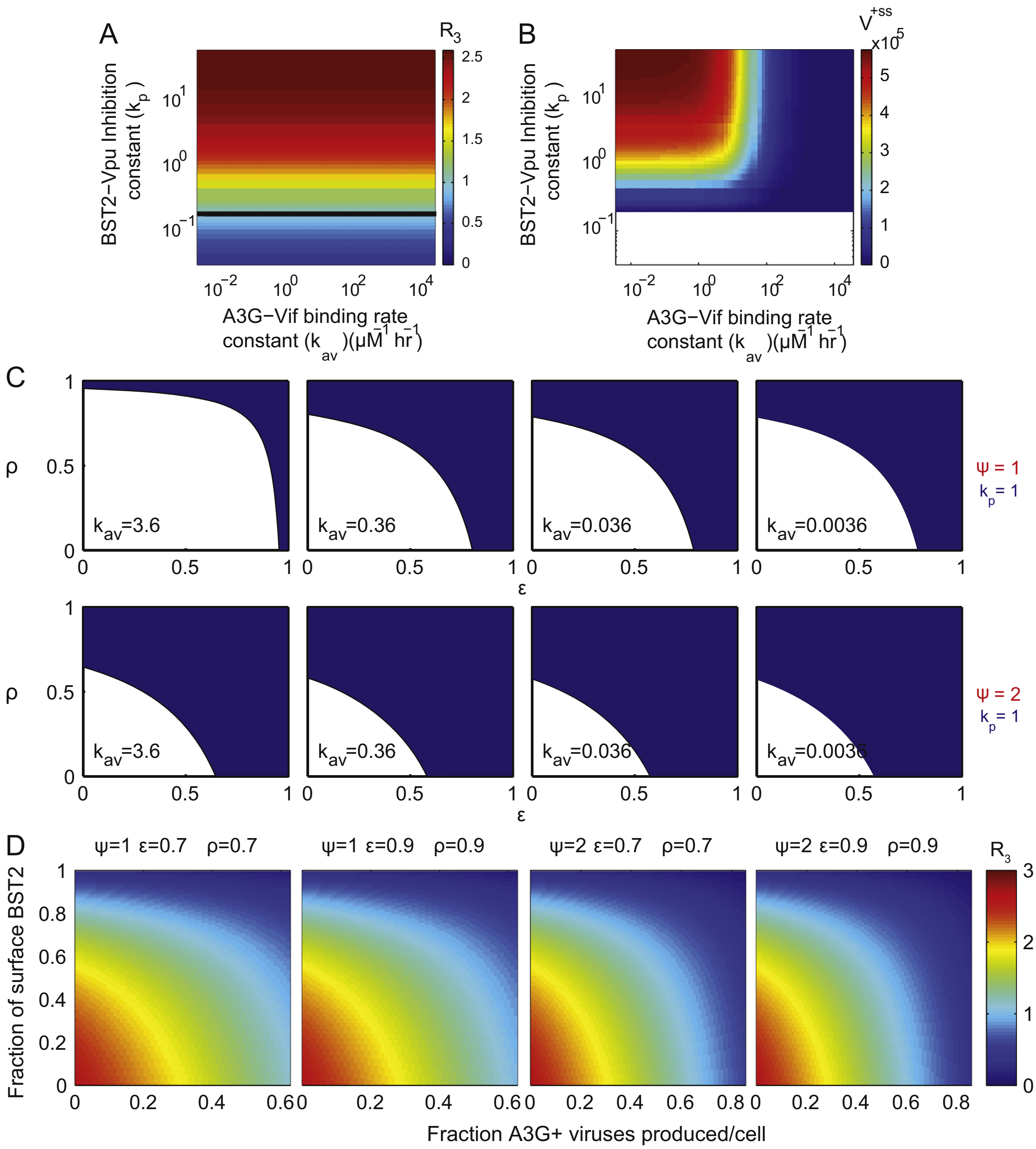

Fig. 7. *HIV-1 dynamics under combination treatment of BST2–Vpu and A3G–Vif.* (A) Heatmap showing the change in the reproductive ratio as a function of BST2–Vpu inhibition constant k_p and A3G–Vif binding rate constant k_{av}, when A3G has no inhibitory activity ($\rho=0$; $\epsilon=0$). (B) Heatmap of the steady-state A3G+ virus population as a function of BST2–Vpu inhibition constant k_p and A3G–Vif binding rate constant k_{av}, when A3G has no inhibitory activity ($\rho=0$; $\epsilon=0$). (C) Area plots in which the shaded area represents the parameter range in which $R_3 < 1$. Each area plot obtained for a binding rate constant value shown in the plot. The calculations were performed for two ψ values 1 (upper panel) and 2 (lower panel). (D) Heatmaps showing R_3 as a function of two different biomarkers fractions of surface BST2 level compared to pre-infection level and fraction of A3G+ virus particle produced per infected cell over the life of the infected cell. Parameter values used to calculate R_3 are $\lambda = 10^4$ ml^{-1} day^{-1}, $\mu = 0.01$ day^{-1}, $\delta(a) = 1$ day^{-1}, $c=23$ day^{-1}, and $k_0 = 2.4 \times 10^{-8}$ ml^{-1} day^{-1}.

various values of ϵ and ρ (Fig. 5E). At high binding rates, varying ϵ and ρ has little influence on R_2 (Fig. 5C and D), but at low binding rates, with a greater number of A3G+ viruses in the system, A3G may have considerable impact on new viral infections.

We further explored the parameter landscape of binding rate constant k_{av}, ϵ and ρ to obtain parameter ranges in which R_2 is less than 1. The parameter ranges for which $R_2 < 1$ is the shaded area (Fig. 5F). Decreasing k_{av} increases this area, indicating that lower values of ϵ and ρ are sufficient to reduce the reproductive ratio below 1 (Fig. 5F). Next, we increased the propensity parameter ψ from 1 to 2 which increases the number of A3G+ viruses produced per cell. We observe that this change in the packaging propensity parameter dramatically affects the parameter range of ϵ and ρ (shaded area), requiring smaller changes in the binding rate constant k_{av} (via a potential A3G targeted therapy) to reduce reproductive ratio below 1 (Fig. 5F lower panel).

2.2.4. *HIV-1 dynamics in the presence of A3G–Vif interaction inhibitors*

Though T cells express A3G, HIV-1 evades its antiviral effect sufficiently to establish an infection. This suggests that HIV-1-Vif provides a strong neutralizing response to A3G activity. We simulated the model (9) with the initial condition that the *in vivo* population of A3G+ viruses to be very low, approximated to

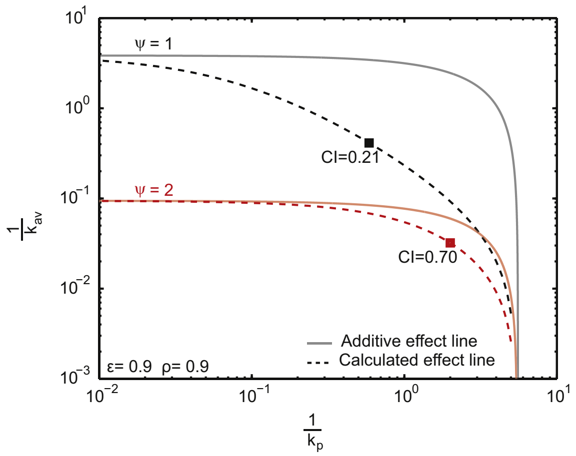

Fig. 8. *Isobologram of BST2–A3G combination therapy plotted on logarithmic scale.* Plot shows model predicted synergy lines (dashed line) obtained after setting $R_3 = 1$ in Eq. (16). It also shows the standard additive effect lines (solid faded lines) obtained by drawing a line joining $1/k_p^E$ and $1/k_{av}^E$. Highest levels of synergy (lowest CI values) are indicated as squares. (For interpretation of the references to color in this figure caption, the reader is referred to the web version of this paper.)

$V^+ = 0$. Hence, the population of infected T cell carrying lethally mutated proviral DNA can be set to $\int_0^\infty T^0(a,t)\,da = 0$, resulting in $V^0 = 0$. Thus only three species exist at pretreatment steady state: uninfected T cells, infected T cells, and virus. (The pretreatment steady-state values are similar to those used for simulating the previous HIV-1 dynamics model with BST2.)

At time zero we start the hypothetical treatment that reduces the A3G–Vif binding rate constant of k_{av} by three fold at time zero. The first simulation is in the condition of no A3G activity (i.e. $\epsilon = 0$ and $\rho = 0$). The results show that the A3G+ virus population emerges following treatment and reaches a new steady-state value (Fig. 6A). The previous A3G− virus population drops and reaches steady state. We see no effect on the total infectious virus population, $V^T = V^- + V^+$, as A3G's antiviral function was set to zero.

Next, we switch on A3G's RT inhibition ($\epsilon = 0.9$) and hypermutation effectiveness ($\rho = 0.9$), but keeping previous k_{av} values. For these values, we see that the virus population drops significantly and oscillates before reaching a new lower steady state (Fig. 6B). Similar behavior is observed for both A3G− and A3G+ virus populations. The uninfected T cell population rises and, after some oscillations, reaches a new steady state value that is higher than the pretreatment value. These simulations show that even with high RT inhibition efficacy and high hypermutation probability HIV-1 manages to escape the A3G effect. However, upon a more severe reduction of the A3G–Vif binding rate, HIV-1 dynamics change dramatically; all virus populations drop and do not show any recovery (Fig. 6C). In this condition, A3G+ infected cell population is substantial and A3G activity influences both number infection events and production of infectious virions. With fewer infected cells to produce viruses, the system fails to replenish the viruses cleared. Due to this imbalance of virus production and clearance, the total virus population drops and never recovers. A recovery from HIV-1 infection can also be seen in the uninfected T cell population that reaches back to the pre-infection steady state value. These results suggest that Vif-targeted treatment can in principle be developed as a possible treatment for HIV-1 infection, though it requires a substantial reduction in the A3G–Vif binding rate.

2.3. Multi-scale model of HIV-1 dynamics shaped by both BST2 and A3G

After studying the role of BST2 and A3G in HIV-1 infection individually, in this section we examine their combined influence. As both models are compatible, the mathematical formulation for the combination treatment remains similar to (9) with a revision to include BST2's effect. BST2 affects the release of both A3G+ and A3G− viruses. As we do not distinguish between A3G+ and A3G− non-infections viruses, the production rate of these viruses can be given by Eq. (4). However, the production rates of infectious viruses are as follows:

$$p_1^-(a) = \begin{cases} \beta(B)(1-\alpha(A))p^*(1-e^{-\theta(a-a_1)}) & \text{if } a \geq a_1 \\ 0 & \text{else} \end{cases}$$

$$p_1^+(a) = \begin{cases} \beta(B)\alpha(A)p^*(1-e^{-\theta(a-a_1)}) & \text{if } a \geq a_1 \\ 0 & \text{else} \end{cases} \tag{15}$$

The steady-state analysis gives us estimates of different variables. The reproductive ratio R_3 under the combined effect of BST2 and A3G can be calculated as follows:

$$R_3 = \frac{\lambda k_0 N_2}{\mu c}$$

$$N_2 = (N_2^- + (1-\epsilon)(1-\rho)N_2^+) \tag{16}$$

where N_2^- and N_2^+ is the total number of A3G− and A3G+ viruses produced in the presence of BST2 by an infected cell in its lifespan. The number can be determined using the following equations:

$$N_2^{\pm} = \int_0^\infty p_1^{\pm} e^{-\int_0^a \delta(s)\,ds}\,da \tag{17}$$

Using the above relations we examine the impact of the combined BST2 and A3G antiviral activity on the reproductive ratio. Fig. 7A shows R_3 as a function of both the BST2–Vpu and A3G–Vif binding rates. Similar to the previous observation, we see that a reduction in k_p has more influence than a reduction in k_{av} when the efficacy parameters $\epsilon = \rho = 0$ (Fig. 7A). However, the steady-state A3G+ virus population increases as the value of k_{av} drops (Fig. 7B). Upon reducing both k_p and k_{av}, both A3G+ virus and total virus population drop as a consequence of reduced per cell virus production. Once the reproductive ratio drops below 1 the steady state virus population drops to zero ceasing infection.

We further studied the impact of RT inhibition and hypermutation in combination with a reduction in the BST2–Vpu inhibition constant. Fig. 7C shows area plots for different binding rate, ϵ and ρ, and inhibition constant reduced by a factor of 3. Comparison between Fig. 7C and Fig. 5F reveals an increase in the shaded area of $R_3 < 1$. The binding rate constant required to achieve a reproductive ratio of less than 1 in the case of A3G-based single therapy is lower compared to combination therapy. We observe a similar effect for ψ=2; a reproductive ratio of <1 can be achieved with less stringent parameters (Fig. 7C lower panel). The implications of varying k_p and k_{av} can also translated into experimentally measurable quantities such as fraction surface BST2 level and fraction of A3G+ viruses produced per cell, respectively. Using these two biomarkers we show the relation between their level and value of reproductive ratio (Fig. 7 D). As shown above, an increase in the surface BST2 level adversely affects the reproductive ratio and increasing per cell A3G+ virus production enhances this effect. Further, simulation results show that for very high A3G anti-viral activity ($\epsilon = \rho = 0.9$) increase in A3G+ virus fraction beyond 0.6 does not offer significant improvement in reducing the reproductive ratio. As seen in the heatmaps, R_3 values change similarly for two packaging propensities. However, at moderate A3G activity ($\epsilon = \rho = 0.7$) increasing A3G+ virus fraction benefits in the reducing R_3. These results indicate that BST2- targeted treatment may improve the effectiveness of A3G-targeted treatment. These calculations indicate that a combination of the BST2- and A3G-based treatments have certain additive effects and complement each other by increasing the overall effectiveness. Simulations of the combination therapy model further illustrate that HIV-1 infection ceases at higher k_p, k_{av} values and lower ϵ, ρ values compared to single host factor treatment values (Supplementary Fig. 2A and B). Thus the model results indicate that a host restriction factor-based HIV-1 therapeutic strategy could contain a mix of agents targeting different mechanisms to improve the overall efficacy. Though solely theoretical, our modeling studies provide a framework to quantitatively assess the influence of host restriction factors on HIV-1 infection dynamics.

2.4. *Combination therapy with synergistic effect*

The above simulation results suggest that targeting BST2 and A3G in a combination therapy may boost the antiviral effect. To analyze whether such therapies might have additive or synergistic effects we considered the scenario in which drop in the A3G–Vif binding rate constant k_{av} and BST2–Vpu inhibition constant k_p are inversely proportional to the drug dosage. In other words, to target the A3G–Vif interaction a drug dose of $1/k_{av}^X$ units and to target the BST2–Vpu interaction a drug dose of $1/k_p^Y$ units is needed to reduce the A3G–Vif binding rate constant to ${k_{av}}^X$ and BST2–Vpu inhibition constant to k_p^Y, respectively. Further, $1/k_p^E$ is the effective concentration of a BST2 targeting drug required to reduce the reproductive ratio$=1$, where ${k_p}^E$ is the effective inhibition constant which gives $R_1=1$ for a mono-therapy targeting BST2–Vpu axis. Similarly, $1/k_{av}^E$ is the effective dose of A3G targeting drug and ${k_{av}}^E$ is the effective binding rate constant that gives value of $R_2=1$ when $\epsilon=\rho=0.9$ for a mono-therapy targeting A3G–Vif axis. For our single therapy models we obtained the values $1/k_{av}^E$ and $1/k_p^E$ for two different A3G propensities ($\psi=1$ and 2). Using these values we draw the additive effect lines (Fig. 8, solid line). Next, for combination therapy, we evaluated the value of k_{av} for different values k_p. Dashed lines in Fig. 8 represent the calculated values of k_{av} for different values k_p that give a reproductive ratio $R_3=1$ for $\psi=1$ (black) or 2 (red) by solving Eq. (16). As both calculated lines are below the additive line we conclude that the combination therapy has a more than additive effect. To further obtain a quantitative estimates of the observed synergy we determined the combination index (CI) for data points on the calculated synergy curve (dashed lines in Fig. 8). Details of the CI calculation are provided in the Methods section. The CI value can be used to determine presence and degree of synergy. CI less than 1 indicates synergism and the smaller the value of CI the stronger is the synergy. CI changes with change in k_{av} and k_p and as the effect of one host factor therapy fades CI climbs toward 1 (Supplementary Fig. 3). For low propensity ($\psi=1$) CI$=$0.21 (black square symbol in Fig. 8) indicating strong synergism (Chou, 2006), and for high A3G propensity ($\psi=2$) CI$=$0.70 (red square symbol in Fig. 8) indicating moderate synergism. These CI values show that the degree of synergism decreases with an increase in A3G's packaging propensity. This may be rationalized, by the fact that an increased fraction of A3G+ viruses reduce the number of successful infections and subsequent secondary infections, diminishing the effect of BST2 on viral release. However, as CI values are generally less than 1, we conclude that a BST2–A3G combination therapy would generally have a synergistic therapeutic effect.

3. Discussion

HIV-1 is known to evade both innate and adaptive immune defences to establish a chronically active infection. Over the last two decades, we have gained considerable understanding of the functions of HIV-1 accessory proteins in counteracting host innate immune defenses by interacting with and neutralizing key antiviral host factors. However, whether HIV-1 accessory proteins may serve as promising drug targets to complement existing therapeutic modalities focused on HIV-1 core proteins remains unclear.

Here, we have developed a multi-scale modeling framework to evaluate the promise of pharmacologically targeting the HIV-1 accessory proteins Vpu and Vif, which target the host restriction factors, BST2 and A3G, respectively. These models describe the *in vivo* HIV-1 dynamics as a function of the intracellular kinetics of host factors and their viral inhibitors. Simplifying the multi-scale formulation we derived analysis-amenable equations to explore regions of the parameter landscape wherein therapy can succeed. To the best of our knowledge, ours is the first study that uses multi-scale modeling of *in vivo* HIV-1 dynamics coupled to the intracellular kinetics of host restriction factors and accessory proteins. Further, we provide a framework that may be extended to include other host resistance factors and their HIV-1 accessory protein counterparts and enable evaluation of their pharmacological targeting, as well as the efficacy of combination therapies exploiting them.

Our HIV-1 dynamics model is based on previous studies that have successfully captured the *in vivo* disease progression and have guided the evaluation of HIV-1 core-protein-based therapies (Perelson et al., 1996; Dixit et al., 2004; Perelson et al., 1997; Stafford et al., 2000). Similarly, we hope our multi-scale model framework is useful in guiding therapeutic development aimed at HIV-1 accessory proteins. The availability of further *in vitro* and *in vivo* experimental data will allow iterative improvements to the model and the insights gleaned from its use.

Using the concept of the basic reproductive ratio, we demonstrated that the Vpu-induced downregulation of BST2 affects the survival of the virus. We found that given experimentally informed HIV-1 dynamics parameters, an infected cell has to retain around 85% (0.85 in fraction) of BST2 in order to bring the reproductive ratio below 1. To obtain these estimates, we used published experimental data sets (Schmidt et al., 2011; Mangeat et al., 2009) and established correlations for BST2 expression, Vpu-induced downregulation, and virus restriction. In order to maintain such BST2 levels, Vpu activity and degradation of BST2 must be low, and our model provides a benchmark for how effective inhibitors of Vpu activity must be if they are to restrict the progression of HIV-1 infection *in vivo*. We also found a non-linear relationship between per cell virus production and critical surface BST2 level.

We next considered the host restriction factor, A3G, which not only inhibits the RT process, but also introduces hypermutations that render progeny viruses defective. The multi-step mechanism of A3G antiviral activity required additional species within the age-structured *in vivo* HIV-1 dynamics model. Model simulations provided a quantitative illustration of the fact that A3G has to succeed at two steps of its mode of action. First A3G has to be efficiently packaged into a large fraction of budding viruses, and second it must either effectively block the RT process or induce lethal mutations in a large number of RT events. However, only if A3G is packaged in a majority of progeny viruses will the reproductive ratio drop below 1. Thus A3G-based antiviral therapies should not only aim at reducing the A3G–Vif interaction, but also increase the propensity of A3G to package into budding viruses. This point may be accentuated when considering that A3G activity may result in mutations that accelerate the development of drug resistance (Hache et al., 2006; Jern et al., 2009). With the availability of relevant experimental data, our modeling framework may be expanded in further studies to address a potential role of A3G in drug resistance and its implications for Vif-targeted drug development.

We also model the combined BST2 and A3G activities in order to explore their interactions. Model results show that the implementation of BST2–Vpu treatment does improve the overall performance of A3G-based interventions. Side-effects are often detrimental in drug treatment and cause non-adherence to therapy. Hence, minimal dosages that minimize side-effects are usually preferable. Multi-drug therapies may allow for synergistic efficacies at lower drug doses with minimal side-effects while maintaining therapeutic benefits. Using the model we assessed the impact of combined targeting of Vpu and Vif by combination therapy, both qualitatively using isobolograms and quantitatively by calculating the combination index CI. Our results indicate that the level of synergy is determined by the effectiveness of A3G (Fig. 8). Specifically, highly effective A3G therapy is predicted to reduce the boost gained from concurrent BST2-targeted treatment. Using this analysis of CI values, we can obtain optimal model parameters values that would provide the highest synergy in combination therapy. We note that BST2–Vpu-based therapy reduces the total viral production and thus the number of RT events, potentially reducing the risk of producing A3G-induced drug resistant strains. Thus, we propose that BST2-targeted treatment may augment A3G targeted treatment in more than one way.

In this work we made predictions using the concept of the reproductive ratio to evaluate the effectiveness of host restriction factors when accessory proteins are inhibited. To extend the analytical treatment we also numerically solved the model equations and explored the resulting dynamics of HIV-1 infection. Changes in virus and cell populations over time provided information about the efficiency of BST2 function in viral release, A3G packaging, and the two A3G functions in RT inhibition and hypermutation. Our results show that if treatment fails to bring the reproductive ratio below 1 it causes a transient perturbation that leads to new steady state of continued viral replication. However, when treatment succeeds in reducing the reproductive ratio below 1, the population drops steadily and the system regains an infection-free steady state.

HIV-1 remains latent in resting memory CD4$^+$ T cells having very long half-life. These cells remain undetectable to the immune systems and provide a long lived source of HIV-1. Activation of these resting cells initiates replication of latent HIV leading to virus production. In addition, these cells are responsible for very low level of virus replication. Hence, removal of drug therapy has high probability of viral load rebound. Rong and Perelson after reviewing different models found that earlier HIV viral dynamics models did not include population of latently infected T cells (Rong and Perelson, 2009). Although these models can successfully capture the two phase decline in the viral load, they are unable to capture the low-level persistent viral load. Another study shows that the low-level viral replication can be captured by including the latently infected T cell population into the standard HIV dynamics model (Rong and Perelson, 2009). Similarly, our current model can further be advanced by incorporating latent infected T cell population to study the long term effects of HIV-1 accessory proteins targeting therapies.

In summary, we have presented a mathematical formulation that links intracellular kinetics of cell/virus protein interactions with cell/virus population dynamics. This framework may be used to evaluate therapeutic strategies that target HIV-1 accessory proteins and facilitate anti-viral activity of host factors. The framework is extendable and other host restriction factors and viral accessory proteins may be included in future studies. As the modeling framework is based on prior work focused on therapies targeting HIV-1 core proteins, it is also amenable to evaluating combination therapies that include both HIV-1 core and accessory protein inhibitors, and guide the use of complex treatment regimes.

4. Methods

4.1. BST2–Vpu intracellular kinetics

Values for protein production and degradation parameters were taken from the literature (Hosseini and mac Gabhann, 2012), and we assume that both HIV-1-Vpu and HIV-1-Vif have similar production and degradation rates.

We used two separate data sets from the literature to estimate different parameters. BST2 internalization data was collected by monitoring the down regulation of surface BST2 in uninfected cell (Perez-Caballero et al., 2009) and we used this data to obtain parameter, μ_B. In these experiments, internalization measurements were unaffected by recycling and an exponential decay model is sufficient to obtain value of μ_B from this data (Supplementary Fig. 4). Normalization of the BST2 equation (1) with infection free surface BST2 level enables estimation of λ_B. Next, we made the Vpu model concentration-independent, which allowed us to solve the equations with fewer parameters and to obtain dimensionless values for both BST2 and Vpu with respect to infection age. We link the BST2 surface level to virus restriction efficiency and for this we use another set of experimental data that measured both BST2 levels and its impact on the virus release (Mangeat et al., 2009). For this second data set BST2 level of the infected cell in the first round of infection was measured and virus supernatant was used for infectivity assays. We assume that band intensities of immunoblots and fluorescence intensities are proportional to the quantities it measured. Using this data we obtained the relation between the dimensionless BST2 level and restriction efficiency (correlation equation and data used for it are shown in Fig. 1B). We numerically solved the dimensionless BST2 and Vpu equations.

4.2. A3G–Vif intracellular kinetics

We numerically solved Eq. (7) and obtained profiles of A3G and Vif change as a function of age of an infected cell and also calculated the fraction of A3G+ virus produced by the infected cell for different concentrations of A3G (Fig. 4B) (Supplementary Fig. 1B shows the effect of change in ψ and binding rate constant on k_{av} on steady-state A3G+ virus population). The parameters of A3G–Vif kinetics were taken from the published modeling study (Hosseini and mac Gabhann, 2012).

4.3. Analysis of HIV-1 dynamics model

In the equation system (3), we obtain the analytical solution of the PDE as follows:

$$T^*(a,t) = k_0 V(t-a) T(t-a) e^{-\int_0^a \delta(s)\,ds} \tag{18}$$

For convenience, henceforth, we use the following term:

$$\Lambda(a) = e^{-\int_o^a \delta(s)\,ds} \tag{19}$$

The steady-state levels of the uninfected T cell population and virus population are obtained by setting the time derivative terms equal to zero and the equations can be written as follows:

$$0 = \lambda - \mu T^{SS} - k_0 V^{SS} T^{SS}$$

$$0=\int_0^\infty p(a)k_0V^{SS}(t-a)T^{SS}(t-a)\Lambda(a)\,da-cV^{SS} \tag{20}$$

Solving these equations gives us the following output:

$$k_0V^{SS}T^{SS}=\lambda-\mu T^{SS} \tag{21}$$

substituting above into the steady state virus equation (20) we obtain

$$T^{SS}=\frac{c}{k_0N} \tag{22}$$

where $N=\int_0^\infty p(a)\Lambda(a)\,da$ is the total number of viruses produced by an infected cell over its life span. After substituting the T^{SS} in the steady state uninfected T cell equation (20) we obtain the following equation of steady-state virus load:

$$V^{SS}=\frac{\lambda k_0N-\mu c}{k_0c} \tag{23}$$

Infected steady state, $V^{SS}>0$, can be possible if and only if $(\lambda k_0N-\mu c)>0$, which gives us the following constant:

$$R_O=\frac{\lambda k_0N}{\mu c} \tag{24}$$

For an infection-free steady state with no virus present in the system, $V^{SS}=0$, the uninfected T cell population reaches a value $T^{SS}=\lambda/\mu$. For all models presented in this work a similar procedure is followed to obtain the steady-state values.

For calculating the numerical values of R_O we use Simpson's 1/3 rule to evaluate the virus number produced per cell N. The same method is applied for the calculation of all the reproductive ratios. We used MATLAB to code Simpson's rule for these calculations. For numerical simulations of the HIV-1 model equations we first use the method of characteristics to transform the PDE into the following ODE

$$\frac{d}{da}T^*=-\delta(a)T^* \tag{25}$$

where the initial condition for this ODE is $T^*(0)=k_0V(t)T(t)$. We integrate all differential equations of HIV-1 dynamics using Runge–Kutta fourth order method as it is best suited, considering the coupled nature of our ODEs and PDEs. We first integrate ODEs of uninfected T cell and virus population and obtain their values for time step $t+\Delta t$. We then use this value to integrate the ODEs of infected T cell population. We use Simpson's 1/3 rule to calculate the integral in the virus equation. As our intracellular kinetics equations are not directly coupled into the HIV-1 dynamics, we solve the ODEs of intercellular kinetics, using LSODA ODE solve package, prior to solving the HIV-1 dynamics equations. This way we obtain profiles for $\beta(B)$ and $\alpha(A)$ as a function of age of infection. We use these profiles while evaluating the integral term in virus population equation. A Fortran code was written to implement these numerical techniques. Supplementary tables provide list of the model variables and parameter with units and their values used for the simulations.

4.4. Isobologram and combination index (CI)

Isobolograms are used to depict the existence of synergism, additive effect and antagonism observed in combination drug treatments (Chou, 2006; Berenbaum, 1989; Chou and Talalay, 1983). For our study, we assume that a drop in binding rate constant and inhibition constant to be proportional to the concentration of drug dose. Thus, the isobologram y-axis is $1/k_{av}$, representing dosage of a A3G–Vif targeting drug, and the x-axis is $1/k_p$ values, representing dosage of a BST2–Vpu targeting drug. The therapeutic effectiveness is measured by calculating the reproductive ratio. The parameters $1/k_{av}^E$ and $1/k_p^E$ are single therapy dosages that give $R_2=1$ and $R_1=1$, respectively. A straight line joining point $1/k_{av}^E$ (y intercept) and $1/k_p^E$ (x intercept) on a linear x–y plot represents the additive effect line (in Fig. 8 continuous line represents additive effect). When the A3G/BST2 combined effect value lies above the additive line the two drugs are antagonistic, when the effect value lies below they are synergistic. We computed the combination index CI based on Chou and Talalay (1983) and Chou (2006) to accommodate our definition of drug dosage. Our formula for calculation of CI is as follows:

$$CI=\frac{(1/k_{av})}{(1/k_{av}^E)}+\frac{(1/k_p)}{(1/k_p^E)} \tag{26}$$

where k_{av} is the binding rate constant computed for a given value of k_p with reproductive ratio R_3 set to 1. Supplementary Fig. 3 shows a 3D line plot of CI values as a function of both $1/k_p$ and $1/k_{av}$.

Acknowledgements

We thank John Young, Sumit Chanda, Rick Bushman, and Alan Perelson for helpful discussions. This work is supported by NIH grant P01-AI090935-01.

Appendix A. Supplementary data

Supplementary data associated with this paper can be found in the online version at http://dx.doi.org/10.1016/j.jtbi.2015.08.032.

References

Alce, T.M., Popik, W., 2004. APOBEC3G is incorporated into virus-like particles by a direct interaction with HIV-1 Gag nucleocapsid protein. J. Biol. Chem. 279 (August (33)), 34083–34086, URL http://dx.doi.org/10.1074/jbc.C400235200.

Althaus, C.L., de Boer, R.J., 2010. Intracellular transactivation of HIV can account for the decelerating decay of virus load during drug therapy. Mol. Syst. Biol. 6, 348, URL ⟨http://www.ncbi.nlm.nih.gov/pubmed/20160709⟩.

Althaus, C.L., de Vos, A.S., de Boer, R.J., 2009. Reassessing the human immunodeficiency virus type 1 life cycle through age-structured modeling: life span of infected cells, viral generation time, and basic reproductive number, R0. J. Virol. 83 (15), 7659–7667, URL ⟨http://www.ncbi.nlm.nih.gov/pubmed/19457999⟩.

Apolonia, L., Schulz, R., Curk, T., Rocha, P., Swanson, C.M., Schaller, T., Ule, J., Malim, M.H., 2015. Promiscuous RNA binding ensures effective encapsidation of APOBEC3 proteins by HIV-1. PLoS Pathog. 11 (January (1)), e1004609, URL http://dx.doi.org/10.1371/journal.ppat.1004609.

Berenbaum, M.C., 1989. What is synergy? Pharmacol. Rev. 41 (2), 93–141.

Bishop, K.N., Holmes, R.K., Sheehy, A.M., Malim, M.H., 2004. APOBEC-mediated editing of viral RNA. Science 305 (5684), 645, URL ⟨http://www.ncbi.nlm.nih.gov/pubmed/15286366⟩.

Brass, A.L., Dykxhoorn, D.M., Benita, Y., Yan, N., Engelman, A., Xavier, R.J., Lieberman, J., Elledge, S.J., 2008. Identification of host proteins required for HIV infection through a functional genomic screen. Science 319 (5865), 921–926, URL ⟨http://www.ncbi.nlm.nih.gov/pubmed/18187620⟩.

Chou, T.C., 2006. Theoretical basis, experimental design, and computerized simulation of synergism and antagonism in drug combination studies. Pharmacol. Rev. 58 (3), 621–681, URL ⟨http://www.ncbi.nlm.nih.gov/pubmed/16968952⟩.

Chou, T.-C., Talalay, P., 1983. Analysis of combined drug effects: a new look at a very old problem. Trends Pharmacol. Sci. 4, 450–454.

Cocka, L.J., Bates, P., 2012. Identification of alternatively translated tetherin isoforms with differing antiviral and signaling activities. PLoS Pathog. 8 (9), e1002931.

Conticello, S.G., Harris, R.S., Neuberger, M.S., 2003. The Vif protein of HIV triggers degradation of the human antiretroviral dna deaminase apobec3g. Curr. Biol. 13 (22), 2009–2013, URL ⟨http://www.ncbi.nlm.nih.gov/pubmed/14614829⟩.

Dixit, N.M., Markowitz, M., Ho, D.D., Perelson, A.S., 2004. Estimates of intracellular delay and average drug efficacy from viral load data of HIV-infected individuals under antiretroviral therapy. Antivir. Ther. 9, 2, URL ⟨http://www.ncbi.nlm.nih.gov/pubmed/15134186⟩.

Dube, M., Paquay, C., Roy, B.B., Bego, M.G., Mercier, J., Cohen, E.A., 2011. HIV-1 Vpu antagonizes BST-2 by interfering mainly with the trafficking of newly synthesized BST-2 to the cell surface. Traffic 12 (12), 1714–1729, URL ⟨http://www.ncbi.nlm.nih.gov/pubmed/21902775⟩.

Dussart, S., Douaisi, M., Courcoul, M., Bessou, G., Vigne, R., Decroly, E., 2005. APOBEC3G ubiquitination by Nedd4-1 favors its packaging into HIV-1 particles. J.

Mol. Biol. 345 (January (3)), 547–558, URL http://dx.doi.org/10.1016/j.jmb.2004.10.067.

Fauci, A.S., Folkers, G.K., Dieffenbach, C.W., 2013. HIV-AIDS: much accomplished, much to do. Nat. Immunol. 14 (11), 1104–1107, URL ⟨http://www.ncbi.nlm.nih.gov/pubmed/24145780⟩.

Gilchrist, M.A., Coombs, D., Perelson, A.S., 2004. Optimizing within-host viral fitness: infected cell lifespan and virion production rate. J. Theor. Biol. 229 (2), 281–288, URL ⟨http://www.ncbi.nlm.nih.gov/pubmed/15207481⟩.

Gottlinger, H.G., Dorfman, T., Cohen, E.A., Haseltine, W.A., 1993. Vpu protein of human immunodeficiency virus type 1 enhances the release of capsids produced by gag gene constructs of widely divergent retroviruses. Proc. Natl. Acad. Sci. USA 90 (15), 7381–7385, URL http://www.ncbi.nlm.nih.gov/pubmed/8346259.

Guedj, J., Dahari, H., Rong, L., Sansone, N.D., Nettles, R.E., Cotler, S.J., Layden, T.J., Uprichard, S.L., Perelson, A.S., 2013. Modeling shows that the NS5A inhibitor daclatasvir has two modes of action and yields a shorter estimate of the hepatitis C virus half-life. Proc. Natl. Acad. Sci. USA 110 (10), 3991–3996, URL ⟨http://www.ncbi.nlm.nih.gov/pubmed/23431163⟩.

Hache, G., Mansky, L.M., Harris, R.S., 2006. Human APOBEC3 proteins, retrovirus restriction, and HIV drug resistance. AIDS Rev. 8 (3), 148–157, URL ⟨http://www.ncbi.nlm.nih.gov/pubmed/17078485⟩.

Hosseini, I., mac Gabhann, F., 2012. Multi-scale modeling of HIV infection in vitro and APOBEC3G-based anti-retroviral therapy. PLoS Comput. Biol. 8 (2), e1002371, URL ⟨http://www.ncbi.nlm.nih.gov/pubmed/22346743⟩.

Hosseini, I., mac Gabhann, F., 2013. APOBEC3G-augmented stem cell therapy to modulate HIV replication: a computational study. PLoS One 8 (5), e63984, URL http://dx.doi.org/10.1371/journal.pone.0063984.

Jern, P., Russell, R.A., Pathak, V.K., Coffin, J.M., 2009. Likely role of APOBEC3G-mediated G-to-A mutations in HIV-1 evolution and drug resistance. PLoS Pathog. 5 (4), e1000367, URL ⟨http://www.ncbi.nlm.nih.gov/pubmed/19343218⟩.

Khan, M.A., Kao, S., Miyagi, E., Takeuchi, H., Goila-Gaur, R., Opi, S., Gipson, C.L., Parslow, T.G., Ly, H., Strebel, K., 2005. Viral RNA is required for the association of APOBEC3G with human immunodeficiency virus type 1 nucleoprotein complexes. J. Virol. 79 (May (9)), 5870–5874, URL http://dx.doi.org/10.1128/JVI.79.9.5870-5874.2005.

Kirschner, D., Webb, G.F., 1996. A model for treatment strategy in the chemotherapy of AIDS. Bull. Math. Biol. 58 (2), 376–390, URL ⟨http://www.ncbi.nlm.nih.gov/pubmed/8713663⟩.

Konig, R., Zhou, Y., Elleder, D., Diamond, T.L., Bonamy, G.M., Irelan, J.T., Chiang, C.Y., Tu, B.P., de Jesus, P.D., Lilley, C.E., Seidel, S., Opaluch, A.M., Caldwell, J.S., Weitzman, M.D., Kuhen, K.L., Bandyopadhyay, S., Ideker, T., Orth, A.P., Miraglia, L.J., Bushman, F.D., Young, J.A., Chanda, S.K., 2008. Global analysis of host-pathogen interactions that regulate early-stage HIV-1 replication. Cell 135 (1), 49–60, URL ⟨http://www.ncbi.nlm.nih.gov/pubmed/18854154⟩.

Malim, M.H., Bieniasz, P.D., 2012. HIV restriction factors and mechanisms of evasion. Cold Spring Harb. Perspect. Med. 2 (5), a006940.

Malim, M.H., Emerman, M., 2008. HIV-1 accessory proteins—ensuring viral survival in a hostile environment. Cell Host Microbe 3 (6), 388–398.

Mangeat, B., Gers-Huber, G., Lehmann, M., Zufferey, M., Luban, J., Piguet, V., 2009. HIV-1 Vpu neutralizes the antiviral factor Tetherin/BST-2 by binding it and directing its beta-trcp2-dependent degradation. PLoS Pathog. 5 (9), e1000574, URL ⟨http://www.ncbi.nlm.nih.gov/pubmed/19730691⟩.

Mangeat, B., Turelli, P., Caron, G., Friedli, M., Perrin, L., Trono, D., 2003. Broad antiretroviral defence by human APOBEC3G through lethal editing of nascent reverse transcripts. Nature 424 (6944), 99–103, URL ⟨http://www.ncbi.nlm.nih.gov/pubmed/12808466⟩.

Matsui, M., Shindo, K., Izumi, T., Io, K., Shinohara, M., Komano, J., Kobayashi, M., Kadowaki, N., Harris, R.S., Takaori-Kondo, A., 2014. Small molecules that inhibit Vif-induced degradation of APOBEC3G. Virol. J. 11, 122, URL ⟨http://www.ncbi.nlm.nih.gov/pubmed/24986077⟩.

McNatt, M.W., Zang, T., Bieniasz, P.D., 2013. Vpu binds directly to tetherin and displaces it from nascent virions. PLoS Pathog. 9 (4), e1003299, URL ⟨http://www.ncbi.nlm.nih.gov/pubmed/23633949⟩.

Mi, Z., Wang, X., He, Y., Li, X., Ding, J., Liu, H., Zhou, J., Cen, S., 2014. A novel peptide to disrupt the interaction of BST-2 and Vpu. Biopolymers 102 (3), 280–287, URL ⟨http://www.ncbi.nlm.nih.gov/pubmed/24676648⟩.

Mohammadi, P., Desfarges, S., Bartha, I., Joos, B., Zangger, N., Munoz, M., Gunthard, H.F., Beerenwinkel, N., Telenti, A., Ciuffi, A., 2013. 24 hours in the life of HIV-1 in a T cell line. PLoS Pathog. 9 (1), e1003161, URL ⟨http://www.ncbi.nlm.nih.gov/pubmed/23382686⟩.

Neil, S.J., Sandrin, V., Sundquist, W.I., Bieniasz, P.D., 2007. An interferon-alpha-induced tethering mechanism inhibits HIV-1 and Ebola virus particle release but is counteracted by the HIV-1 Vpu protein. Cell Host Microbe 2 (3), 193–203, URL ⟨http://www.ncbi.nlm.nih.gov/pubmed/18005734⟩.

Neil, S.J., Zang, T., Bieniasz, P.D., 2008. Tetherin inhibits retrovirus release and is antagonized by HIV-1 Vpu. Nature 451 (7177), 425–430, URL ⟨http://www.ncbi.nlm.nih.gov/pubmed/18200009⟩.

Nelson, P.W., Gilchrist, M.A., Coombs, D., Hyman, J.M., Perelson, A.S., 2004. An age-structured model of HIV infection that allows for variations in the production rate of viral particles and the death rate of productively infected cells. Math. Biosci. Eng. 1 (2), 267–288, URL ⟨http://www.ncbi.nlm.nih.gov/pubmed/20369971⟩.

Perelson, A.S., Essunger, P., Cao, Y., Vesanen, M., Hurley, A., Saksela, K., Markowitz, M., Ho, D.D., 1997. Decay characteristics of HIV-1-infected compartments during combination therapy. Nature 387 (6629), 188–191, URL ⟨http://www.ncbi.nlm.nih.gov/pubmed/9144290⟩.

Perelson, A.S., Neumann, A.U., Markowitz, M., Leonard, J.M., Ho, D.D., 1996. HIV-1 dynamics in vivo: virion clearance rate, infected cell life-span, and viral generation time. Science 271 (5255), 1582–1586, URL ⟨http://www.ncbi.nlm.nih.gov/pubmed/8599114⟩.

Perez-Caballero, D., Zang, T., Ebrahimi, A., McNatt, M.W., Gregory, D.A., Johnson, M. C., Bieniasz, P.D., 2009. Tetherin inhibits HIV-1 release by directly tethering virions to cells. Cell 139 (3), 499–511, URL http://www.ncbi.nlm.nih.gov/pubmed/19879838.

Pillai, S.K., Abdel-Mohsen, M., Guatelli, J., Skasko, M., Monto, A., Fujimoto, K., Yukl, S., Greene, W.C., Kovari, H., Rauch, A., Fellay, J., Battegay, M., Hirschel, B., Witteck, A., Bernasconi, E., Ledergerber, B., Gunthard, H.F., Wong, J.K., Swiss, H.I.V.C. S., 2012. Role of retroviral restriction factors in the interferon-alpha-mediated suppression of HIV-1 in vivo. Proc. Natl. Acad. Sci. USA 109 (8), 3035–3040, URL ⟨http://www.ncbi.nlm.nih.gov/pubmed/22315404⟩.

Rong, L., Feng, Z., Perelson, A., 2007. Mathematical analysis of age-structured HIV-1 dynamics with combination antiretroviral therapy. SIAM J. Appl. Math. 67 (3), 731–756, URL ⟨http://epubs.siam.org/doi/abs/10.1137/060663945⟩.

Rong, L., Feng, Z., Perelson, A., 2008. Mathematical modeling of HIV-1 infection and drug therapy. In: Applied Optimization, vol. 102. Springer Berlin Heidelberg, pp. 87–131 (Book Section 3).

Rong, L., Guedj, J., Dahari, H., Coffield, D.J.J., Levi, M., Smith, P., Perelson, A.S., 2013. Analysis of hepatitis C virus decline during treatment with the protease inhibitor danoprevir using a multiscale model. PLoS Comput. Biol. 9 (3), e1002959, URL ⟨http://www.ncbi.nlm.nih.gov/pubmed/23516348⟩.

Rong, L., Perelson, A.S., 2009. Modeling HIV persistence, the latent reservoir, and viral blips. J. Theor. Biol. 260 (2), 308–331.

Rong, L., Perelson, A.S., 2009. Modeling latently infected cell activation: viral and latent reservoir persistence, and viral blips in HIV-infected patients on potent therapy. PLoS Comput. Biol. 5 (10), e1000533.

Schäfer, A., Bogerd, H.P., Cullen, B.R., 2004. Specific packaging of APOBEC3G into HIV-1 virions is mediated by the nucleocapsid domain of the gag polyprotein precursor. Virology 328 (October (2)), 163–168, URL http://dx.doi.org/10.1016/j.virol.2004.08.006.

Schmidt, S., Fritz, J.V., Bitzegeio, J., Fackler, O.T., Keppler, O.T., 2011. HIV-1 Vpu blocks recycling and biosynthetic transport of the intrinsic immunity factor CD317/tetherin to overcome the virion release restriction. mBio 2 (3), e00036–e00311, URL ⟨http://www.ncbi.nlm.nih.gov/pubmed/21610122⟩.

Sheehy, A.M., Gaddis, N.C., Malim, M.H., 2003. The antiretroviral enzyme APOBEC3G is degraded by the proteasome in response to HIV-1 Vif. Nat. Med. 9 (11), 1404–1407, URL ⟨http://www.ncbi.nlm.nih.gov/pubmed/14528300⟩.

Soros, V.B., Yonemoto, W., Greene, W.C., 2007. Newly synthesized APOBEC3G is incorporated into HIV virions, inhibited by HIV RNA, and subsequently activated by RNase H. PLoS Pathog. 3 (February (2)), e15, URL http://dx.doi.org/10.1371/journal.ppat.0030015.

Stafford, M.A., Corey, L., Cao, Y., Daar, E.S., Ho, D.D., Perelson, A.S., 2000. Modeling plasma virus concentration during primary HIV infection. J. Theor. Biol. 203 (3), 285–301, URL ⟨http://www.ncbi.nlm.nih.gov/pubmed/10716909⟩.

Thangavelu, P.U., Gupta, V., Dixit, N.M., 2014. Estimating the fraction of progeny virions that must incorporate APOBEC3G for suppression of productive HIV-1 infection. Virology 449, 224–228, URL ⟨http://www.ncbi.nlm.nih.gov/pubmed/24418556⟩.

Tokarev, A.A., Munguia, J., Guatelli, J.C., 2011. Serine-threonine ubiquitination mediates downregulation of BST-2/tetherin and relief of restricted virion release by HIV-1 Vpu. J. Virol. 85 (1), 51–63.

van Damme, N., Goff, D., Katsura, C., Jorgenson, R.L., Mitchell, R., Johnson, M.C., Stephens, E.B., Guatelli, J., 2008. The interferon-induced protein BST-2 restricts HIV-1 release and is downregulated from the cell surface by the viral Vpu protein. Cell Host Microbe 3 (4), 245–252, URL ⟨http://www.ncbi.nlm.nih.gov/pubmed/18342597⟩.

Wang, T., Tian, C., Zhang, W., Luo, K., Sarkis, P.T.N., Yu, L., Liu, B., Yu, Y., Yu, X.-F., 2007. 7SL RNA mediates virion packaging of the antiviral cytidine deaminase APOBEC3G. J. Virol. 81 (December (23)), 13112–13124, URL http://dx.doi.org/10.1128/JVI.00892-07.

Xu, H., Chertova, E., Chen, J., Ott, D.E., Roser, J.D., Hu, W.S., Pathak, V.K., 2007. Stoichiometry of the antiviral protein APOBEC3G in HIV-1 virions. Virology 360 (2), 247–256, URL ⟨http://www.ncbi.nlm.nih.gov/pubmed/17126871⟩.

Zhou, H., Xu, M., Huang, Q., Gates, A.T., Zhang, X.D., Castle, J.C., Stec, E., Ferrer, M., Strulovici, B., Hazuda, D.J., Espeseth, A.S., 2008. Genome-scale RNAi screen for host factors required for HIV replication. Cell Host Microbe 4 (5), 495–504, URL ⟨http://www.ncbi.nlm.nih.gov/pubmed/18976975⟩.

Zuo, T., Liu, D., Lv, W., Wang, X., Wang, J., Lv, M., Huang, W., Wu, J., Zhang, H., Jin, H., Zhang, L., Kong, W., Yu, X., 2012. Small-molecule inhibition of human immunodeficiency virus type 1 replication by targeting the interaction between Vif and ElonginC. J. Virol. 86 (10), 5497–5507, URL ⟨http://www.ncbi.nlm.nih.gov/pubmed/22379088⟩.